

Alma Mater Studiorum - Università di Bologna

SCHOOL OF ENGINEERING

- Forlì Campus -

SECOND CYCLE MASTER'S DEGREE IN INGEGNERIA
AEROSPAZIALE/AEROSPACE ENGINEERING

Class: LM-20

Graduation Thesis

in Orbital Dynamics

**Ephemeris generation of the Galilean moons
by using VLBI observations in support to
stellar occultations**

Candidate:

Gianmarco Broilo

Supervisor

Prof. Marco Zannoni

Co-Supervisor

Prof. Dominic Dirkx

Academic Year 2021/2022

*Whatever happens, it will
be a great journey*

Abstract

Stellar occultations are the most accurate Earth-based astronomy technique to obtain the lateral position of celestial bodies, in the case of natural satellites, their accuracy also depends on the central body to which the satellite orbits. The main goal of this thesis work is to analyze if and how very long baseline interferometry (VLBI) measurements of a body like Jupiter can be used in support to stellar occultations of its natural satellites by reducing the planetary uncertainty at the time of the occultation. In particular, we analyzed the events of the stellar occultations of Callisto (15.01.2024) and Io (02.04.2021). The stellar occultation of Callisto has been predicted and simulated using the stellar occultation reduction analysis (SORA) toolkit while the stellar occultation of Io has been already studied by Morgado et al. We then simulated the VLBI data of Jupiter according to the current JUNO trajectories. The required observation were then used as input of an estimation to which then we performed a covariance analysis on the estimated parameters to retrieve the formal errors ($1 - \sigma$ uncertainties) at each epoch of the propagation. The results show that the addition of the VLBI slightly improves the uncertainty of Callisto even when Jupiter knowledge is worse while for Io we observed that the VLBI data is especially crucial in the scenario of an a priori uncertainty in Jupiter state of about 10km. Here we can have improvements of the estimated initial states of Io of about 70m, 230m and 900m to the radial, along-track and cross-track directions respectively. Moreover, we have also obtained the propagated errors of the two moons in terms of right ascension and declination which both show uncertainties in the mas level at the occultation time. Finally, we simulated Io and Europa together and we observed that at the time of the stellar occultation of Europa the along-track component of Io is constrained, therefore confirming the strong coupling between the two inner moons.

Contents

List of Figures	7
List of Tables	9
1 Introduction	11
1.1 The Galilean moons	12
2 Stellar Occultations	15
2.1 Data Analysis	16
2.1.1 Limb fitting	17
2.2 Previous occultations of the Galilean moons	18
3 VLBI	21
3.1 VLBI system	21
3.1.1 Delta VLBI	22
3.2 Sources of error	23
3.3 Delay Model	23
3.3.1 VLBI delay model	25
3.3.2 Estimation of spacecraft state vector	26
3.4 Improvements of Jupiter ephemeris using VLBA astrometry of spacecraft	27
4 State Estimation	29
4.1 Linear Weighted Least squares	31
4.1.1 Variational Equations formulation	33
4.2 Propagation of the covariance matrix	34
4.2.1 Covariance Matrix transformation	35
5 Dynamical Model	39
5.1 States Formulation and Geometry	39
5.2 Data type	40
5.2.1 Data quality and weights	41
5.3 Moon uncertainty simulation	42
5.3.1 Estimated parameters	42
5.3.2 Covariance analysis	42
5.3.3 A priori knowledge	43
5.3.4 Moon Dynamics	44
5.3.5 Propagation and Integration	45

5.3.6	Observation schedule	47
5.4	Covariance propagation	48
5.4.1	Workflow visualization	49
6	Results	53
6.1	Callisto analysis	53
6.1.1	Callisto Occultation	53
6.1.2	Ephemeris results	59
6.2	Io Analysis	63
6.2.1	Ephemeris results	64
6.3	Discussion	69
6.3.1	Considerations of the coupling between Io and Europa	74
7	Conclusions	77
	References	79
A	Procedure to calculate the stabilized a priori covariance	83
B	Output of SORA for the stellar occultation of Callisto	87

List of Figures

1.1	Galilean moons, from left to right: Io, Europa, Ganymede and Callisto; credits to NASA/JPL	13
2.1	Normalized light curve for Ganymede. Bottom image is a close up 30 seconds before/after the occultation [5]	17
2.2	Occultations by 501,502 and 503 taken from [5]	19
3.1	Geometry of observation, [28]	22
3.2	VLBI geometry, [26]	26
4.1	Gaussian distribution, [38]	30
4.2	RSW reference frame	36
4.3	Geocentric equatorial reference system, [44]	36
5.1	General geometry of the observation where the origin corresponds to Earth. The vector r_i corresponds to the position of the $i - th$ moon with respect to Earth while the vector r_i^J expresses the position of the moon with respect to the barycenter of Jupiter.	40
5.2	LEFT: Latitude RIGHT: Longitude; the scale is in the order of 10^{-16}	45
5.3	trajectory of JUNO spacecraft between 2017 and 2021, obtained with SPICE (DE441 and jup365 spice kernels)	48
5.4	Workflow from left to right for the estimation of the initial states; with TudatPy	50
5.5	Workflow for the stellar occultation prediction and analysis; with SORA	51
6.1	Occultation map by 504	54
6.2	Fitted limb on 504	55
6.3	Fitted model	56
6.4	Normalized light curve, 504	56
6.5	Light curve with fitted model	57
6.6	Post fitted model	57
6.7	Geometry of the occultation of Callisto. The red arrow identifies the direction of the velocity vector of Callisto while the black arrow points towards the Earth	58
6.8	Propagated formal errors in case where no data is available	60

6.9	Propagated uncertainties in different scenarios from 6.4. The magenta line indicate the Callisto stellar occultation. For the absolute correlations, elements 0-5 are the state of Callisto, 5-11 Jupiter state, and the other elements on the diagonal are the biases for the stellar occultation and VLBI expressed in terms of right ascension and declination	61
6.10	uncertainties of Callisto in (α, δ) . The magenta line indicates the stellar occultation	63
6.11	Geometry of the stellar occultation of Io	64
6.12	Propagated uncertainties of Io's position in the RSW frame	65
6.13	Propagated uncertainties in different scenarios from 6.4. The magenta line indicate the Io stellar occultation. For the absolute correlations, elements 0-5 are the state of Io, 5-11 Jupiter state, and the other elements on the diagonal are the biases for the stellar occultation and VLBI expressed in terms of right ascension and declination	66
6.14	Absolute difference between case C (only occultation) and case C (occultation and VLBI)	68
6.15	Propagated uncertainties of Io expressed in terms of right ascension and declination (α, δ) . The magenta line indicates the stellar occultation	69
6.16	LEFT: propagated uncertainties of Io RIGHT: propagated uncertainties of Jupiter; the magenta line indicates the stellar occultation while the black line the VLBI observation	71
6.17	Propagated uncertainties in different scenarios of Io (LEFT) and Callisto (RIGHT). The magenta line indicates the stellar occultation	72
6.18	LEFT: propagated uncertainties of Io in right ascension and declination RIGHT: propagated uncertainties of Callisto in right ascension and declination; the magenta line indicates the stellar occultation	73
6.19	LEFT: propagated uncertainties of Io RIGHT: propagated uncertainties of Callisto; the magenta line indicates the stellar occultation	73
6.20	LEFT: propagated uncertainties of Io RIGHT: propagated uncertainties of Europa	75
6.21	LEFT: propagated uncertainties of Io RIGHT: propagated uncertainties of Europa; the magenta line indicates the stellar occultation of Io while the black line the stellar occultation of Europa	75
A.1	LEFT: uncertainties propagation without stabilization RIGHT: uncertainties propagation with stabilization	85

List of Tables

2.1	Fitted times obtained for each light curve, [5]	18
2.2	Final astrometric positions [5]	20
2.3	Offsets in mas between the obtained positions and DE430 ($\Delta RA_1, \Delta Dec_1$) and jup365 ($\Delta RA_2, \Delta Dec_2$) [5]	20
5.1	Propagation and integration parameters	47
6.1	Observation data for body 504	53
6.2	Fitted times	55
6.3	Final predicted astrometric position for Callisto	58
6.4	Callisto analysis of the different scenarios considered in the study	59
6.5	Relative difference in estimated initial states of Callisto expressed in RSW with respect to the case where no data is available. A negative sign indicates an improvement in the uncertainty	62
6.6	Final astrometric position of Io [5]	63
6.7	Io analysis of the different scenarios considered in the study	65
6.8	Relative difference in estimated initial states of Io expressed in RSW with respect to the case where no data is available. A negative sign indicates an improvement in the uncertainty	67

1

Introduction

The highly anticipated JUICE mission (JUperiter ICy moons Explorer) is a spacecraft that will investigate the three Galilean moons Europa, Ganymede and Callisto. According to the current launch scheduled in mid 2023, JUICE will arrive in the Jovian system in 2031. Once it arrives, it will perform many flybys of the moons with the exception of Io: 2 at Europa, 7 at Ganymede at 21 at Callisto, from 2032 to 2034. After, JUICE will initiate its orbital phase around Ganymede [1]. In 2035, the spacecraft will initiate its final circular orbit at 500km for a nominal period of 4 months. The spacecraft will carry 11 experiments, the most important of which are the Planetary Radio Interferometry and Doppler experiment (PRIDE) and the Gravity and Geophysics of Jupiter and the Galilean Moons experiment (3GM). This experiments will be extremely helpful for a more accurate determination of the moon's state [2][3] [4] and improved ephemeris will be used to better understand the long term orbital evolution of the moons which is driven by tidal dissipation in both Jupiter and the satellites. Since Io is not directly observed, optical astrometry data will be crucial in stabilizing the solution for Io. Also, Earth-based astrometry data will be of great importance outside of the JUICE mission in order to provide data set for the positions of the moons. In this work we will investigate the use of stellar occultations as Earth-based technique to obtain astrometric position of natural satellites and therefore generate stable data sets of ephemeris in preparation for future missions. Moreover, improved ephemeris are very important to investigate the origin and evolution of the Jovian system [3] and from the dynamics of the moons it is possible to retrieve information on the dissipation in them. Moreover, studying the dissipation would be very useful to prove and explain the presence of an undersurface ocean on the moons of Europa and Ganymede. These oceans are objects of many studies, especially the ocean of Europa is believed that it could be the only body in the solar system outside Earth to host possible life forms. Furthermore, accurate ephemeris can reduce the uncertainties in future flybys therefore reducing the required ΔV . As we will see, stellar occultation are very accurate measurements with an accuracy as low as 1 mas [5]. However, this type of measurements are very sensitive to the position of the central body the satellites are orbiting, therefore errors in the ephemeris need to be reduced at the time of the occultation. In this work it will be analyzed if and how very long baseline interferometry (VLBI) observations can be

used around the period of a stellar occultation to improve the planetary ephemeris at the time of the occultation. To do so we will perform numerical simulations to create a dynamical model and generate the required observations. We will limit ourselves to a covariance analysis and we will focus on the formal uncertainties. As we will investigate, stellar occultations events for the Galilean moons are rare therefore the possibility to have a VLBI observation close to the stellar occultation time will not always be guaranteed. In this work we will analyze two stellar occultations, in particular the past occultation of Io, already performed by Morgado et al. [5] and we will predict a future stellar occultation of Callisto using the SORA toolkit. VLBI data will be made available by the current JUNO spacecraft, which will be orbiting Jupiter at the time of both occultations. We will also consider the case where no VLBI observations are made to investigate how this will influence the satellite uncertainties. In this work, we will not model the spacecraft as it will be outside the scope of this work, but we will only consider the post processed final observation of the planet.

This work is divided as follows: in Chapter 2 we will analyze the process to obtain final astrometric positions from stellar occultation data and we will see the results for the Galilean moons in the past observational campaign. In Chapter 3, VLBI techniques will be explained in details in addition to the current contribution of the JUNO spacecraft to the improvements of Jupiter ephemeris. Next, in Chapter 4 we will quickly go through the estimation framework as it will be crucial in understanding the covariance analysis of the estimated parameters. In Chapter 5 we will discuss the dynamical model used in the simulations, as well as the propagation and integration of the governing equations. In Chapter 6 we will discuss the results of the moon ephemeris obtained from the covariance analysis and different scenarios will be evaluated. Moreover, we also predicted and simulated a stellar occultation of Callisto with the aid of the Python toolkit SORA, designed to analyze stellar occultations. Finally, in Chapter 6 we will discuss the results and compare the formal uncertainties obtained for Callisto and Io. Moreover, we will also briefly investigate the combination of the two inner satellites of Io and Europa, to see if a stellar occultation of Europa can constrain the uncertainties of Io.

1.1 The Galilean moons

We will now have a brief overview of the Galilean moons which orbit Jupiter, the largest planet in the solar system. The Galilean moons are the four largest moon of Jupiter and they are: Io, Europa, Ganymede and Callisto. They were first observed by Galileo Galilei in 1609 and they were identified as satellites of Jupiter in 1610. The moons have very interesting features. For example, Io which is the closest moon to Jupiter at a distance of 420,000km from the surface, is the most volcanically active body in the solar system, due to its tidal interaction with Jupiter [6]. Europa, which is the second moon of Jupiter, has become interesting since an analysis from Hubble space telescope and the Galileo mission detected water vapor plumes emitted from its surface [7], this is a very important evidence of the liquid ocean beneath the crust of Europa. This discovery along with the strong tidal dissipation within the moon makes it a very promising environment for the development of life in

the solar system [8]. Further, Ganymede is the largest moon in the solar system, even larger than the planet Mercury. Moreover, along with Earth and Mercury is one of the three solid bodies in the solar system that generate a magnetic dipole field [9]. Lastly, at a radial distance of 1,860,000 km, Callisto is the farthest moon with respect to Jupiter. Its topographic feature is that it has the most cratered surface in all the solar system [10] and thanks to the Galileo spacecraft, an induced magnetic field has been detected. It is also believed that underneath the outer icy shell of Callisto a large liquid reservoir is present [11].



Figure 1.1: Galilean moons, from left to right: Io, Europa, Ganymede and Callisto; credits to NASA/JPL

A very particular feature of the first three moons (Io, Europa and Ganymede) is that they follow a specific orbital pattern, which is called Laplace resonance [12]:

$$n_{Io} - 3n_{Europa} + 2n_{Ganymede} = 0 \quad (1.1)$$

Where n is the mean motion of the moon, usually defined as $n = \sqrt{\frac{\mu}{a^3}}$. The first three moons are therefore in a 4:2:1 orbit period ratio, this clearly implies a strong correlation in their dynamics. The exact origin of this resonance is still not very clear and it is also not clear whether is stable or not [8]. One of the main consequences of the resonance is tidal dissipation on the moons, in particular on Io. Nowadays, many solutions of the motion of the moons do not agree in the amount of dissipation and the dynamical evolution of the satellites: for example Layney et al. [13] found that the acceleration due to tides have induced a shift in the position of the moons of about 55km for Io, -125km for Europa and -365km for Ganymede over the past 116 years. These result shows that Io's orbit is reducing while the orbit of Europa and Ganymede are expanding [13]. Moreover, this result shows that the Galilean moons could escape from the Laplace resonance, with great consequences on the tidal dissipation in Io and Europa. On the contrary, a more recent study conducted by Lari [14] showed that on a very long time scale the tidal dissipation results in an orbit increase for all the satellites. After 4 million years, Io will stop to move inwards and will start to migrate outwards.

This interesting result could indicate that the Laplace resonance is a quite new phenomenon and has yet to reach an equilibrium condition [14]. From this brief overview of the Galilean moons we can clearly see the crucial role of accurate data on their state, as it will benefit both future missions and the current research.

2

Stellar Occultations

A stellar occultation occurs when a solar system object passes in front of a star, as seen from Earth [15]. This passage will cause a drop in the observed flux of the star. With this technique it is possible to determine the shape and size of the occulting body [16], and also detect topographic features [17]. Moreover, stellar occultations provide very accurate astrometric measurements that are right ascension α and declination δ of the occulting body, with uncertainties that can be as low as 5-10 km or even smaller for some objects [18]. For the Galilean moons this uncertainty can be as low as 3 km at Jupiter's distance [5]. This uncertainty is order of magnitude lower than classical charged-coupled device (CCD) astrometry because in the case of Jupiter's moon, the brightness of Jupiter would quickly saturate the CCD, thus providing position uncertainties between 300-450 km [19]. For the case of the Galilean moons, stellar occultations provide the best ground-based astrometry, comparable with space probes which usually have uncertainties smaller than 5 km [20]. In addition, the obtained positions and sizes are independent of reflectance models which may be the cause of systematic errors [21]. Accurate orbits of the Galilean moons can be used in support of future missions in this system [3] for example the ESA - JUICE and the NASA - Europa Clipper missions, both targeting the Jupiter system and are scheduled to be launched in this decade. Stellar occultation for the Jovian moons are rare since only stars with a magnitude $G = 11.5$ or lower will provide a magnitude drop higher than $\Delta mag = 0.005$ [15]. This drop is otherwise hard to detect with current techniques. During 2019 and 2021, Jupiter had the galactic center at its back, therefore stellar occultations by Io, Ganymede and Europa were completed successfully by organized campaigns. The probability of a Jovian moon to occult a bright enough star will occur again in 2030 [5], when the Jovian system will pass in front of a dense star region. Here, we analyze the methodology used by Morgado et al., available in [15]. This technique takes advantage of the Python library for stellar occultation reduction analysis *SORA*, dedicated to analyze stellar occultations. The stellar occultations that have been considered in this work are the stellar occultation of Callisto predicted on January 15th 2024 and the stellar occultations of Io (02.04.2021) and Europa (22.06.2020).

2.1 Data Analysis

Firstly, stacking images technique and classical photometric pipelines are used to extract the light curves of the occultation. Opaque edges models, including diffraction effects, finite bandwidth, exposure time and stellar diameter were fitted to the star immersion and emersion behind the satellite at the various stations define the occultation chords [5]. Using the known 3D shape of the satellite, is possible to find its limb and fit this limb to the occultation chords. From this fit is possible to obtain the center of figure and the finally determine the astrometric position of the occulting body.

Images analysis

The images obtained from observational campaigns are first converted into .fits file and then corrected for bias and flat-field using standard procedures of the Image Reduction and Analysis Facility *IRAF* [22]. Galilean moons usually have a small magnitude drop [5], because saturation happen before achieving an adequate signal to noise ratio. Since saturation always occurs before achieving an adequate S/N to adequately show the magnitude drop, stacking consecutive images technique in order to increase the signal to noise ratio at the cost of time resolution. Before the stacking technique, the target centroid (x, y) is measured with a 2D circular symmetric Gaussian fit over pixels within one full-width at half maximum from the center [5]. For this step, Platform for Reduction of Astronomical Images Automatically (*PRAIA*) is used. This alignment consists of vertical and horizontal shifts for each image $(\Delta x, \Delta y)$ relative to a chosen reference image which in this case is the first image of each data-set. After the alignment, the number of stacked images is chosen in order to maximize the signal to noise ratio and the time resolution. Differential aperture photometry is then applied via the *PRAIA* package [23]. During the stellar occultation the star and the satellite are blended in the same aperture therefore this combined flux normalized to unity using a polynomial fit before and after the event.

Times and projection in the sky plane

With the retrieved light curve, it is possible to obtain the immersione t_i and emersion times t_e using a standard χ^2 procedure using *SORA* between the observational light curve and the model. The fitted occultation model considers a sharp-edge occultation model convolved with Fresnel diffraction, stellar diameter, CCD bandwidth and finite integration time.

With the aid of the Jovian ephemeris (jup365 and de440) the Gaia EDR3 star position propagated to the date of the predicted stellar occultation, each ingress and egress times are associated with a stellar position relative to the occulting satellite in the sky-plane (f, g) . f, g are measured positively toward local celestial east and celestial north, respectively. Each pair of positions is a chord.

2.1.1 Limb fitting

Each chord extremity is a point where is possible to fit the parameters that define an ellipse: the ellipse center (f_c, g_c) , apparent semi-major axis (a' and the apparent oblateness ($\epsilon' = (a' - b')/a'$ (where b' is the apparent semi-minor axis) and the position angle of the pole P_p of b' . In this study, we consider the satellites' 3D size and shape to be known.

Using the rotational elements of the Galilean satellites so pole coordinates, direction of prime meridian and its time variation) is possible to calculate the geocentric sub-observer latitude ϕ and longitude λ at the occultation epoch. After obtaining the 3D shape it is possible to obtain the its limb and use it to fit the center of the figure. The fit is done via a Monte Carlo approach with uniform distribution of initial guesses to test a large number of simulated central positions. It is possible to compute the chi-squared statistics:

$$\chi^2 = \sum_{i=1}^N \frac{(r_i - r'_i)^2}{\sigma_{r_i}^2} \quad (2.1)$$

Where σ_{r_i} is the radial component of the uncertainty in each chord extremity. Using this approach it is possible to determine the fitted value as the one that minimizes χ^2 and the marginal $1 - \sigma$ error considering the region where $\chi^2 < \chi_{min}^2 + 1$ [24]. The center positions of the ellipse (f_c, g_c) can be converted to astrometric offsets between the occulting object's center of figure and the star's position $(\Delta\alpha\cos\delta, \delta\delta)$. Thanks to the sub-mas accuracy of the Gaia EDR3 catalogs it is possible to obtain high accuracy astrometric positions of the occulting body. The positioning uncertainties are coming from the uncertainties of the fitted center $(\sigma f_c, \sigma g_c)$ and in the propagated star uncertainties. Usually the resulting uncertainties are at the mas level (few kilometers at Jupiter's distance).

The images are analyzed using the technique explained above, for example we show the light curve obtained from Ganymede. In gray we see the light flux of every image, in black the light curve of the stack of 20 consecutive images and in red the fitted occultation model.

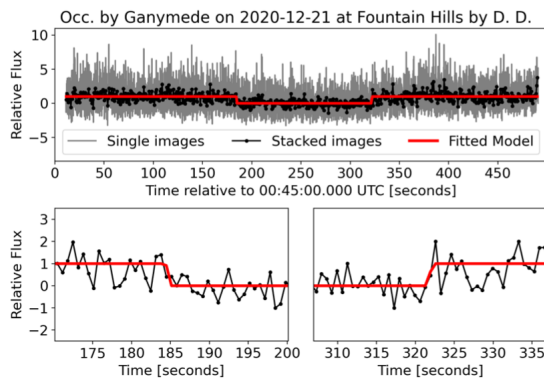


Figure 2.1: Normalized light curve for Ganymede. Bottom image is a close up 30 seconds before/after the occultation [5]

We can now proceed to obtain the observation data and occultation maps for the Io and Europa occultations.

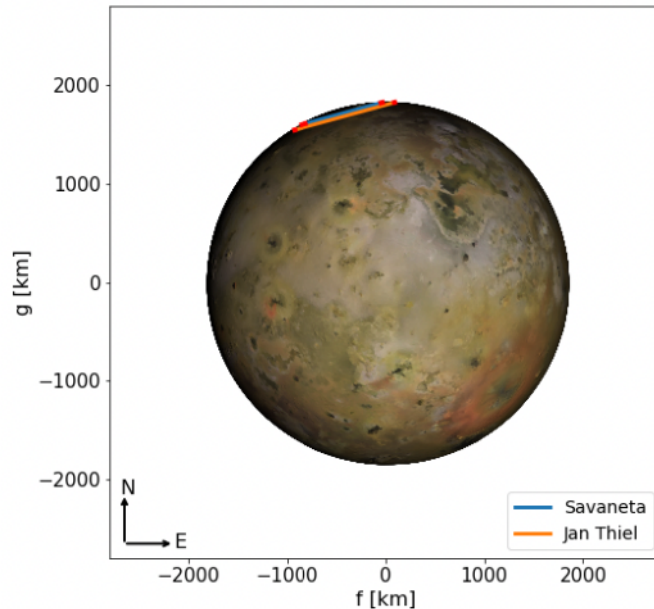
2.2 Previous occultations of the Galilean moons

Morgado et al., conducted successful observational campaigns to observe occultation events of the Galilean moons between 2019 and 2021. In the following table from [5] we highlight the fitted times for the occultations of Io (501), Europa (502) and Ganymede (503).

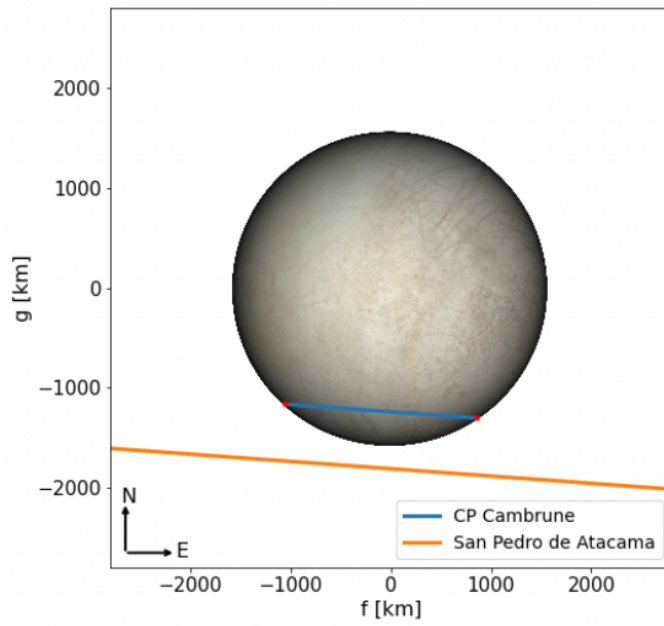
Body	Date and time UTC	immersion time UTC	emersion time UTC	chord length (s)
501	2021-04-02	10:19:54.843 (0.420)	10:20:45.762 (1.278)	50.919 (1.698)
502	2019-06-04	02:28:05.033 (0.044)	02:29:14.311 (0.040)	069.278 (0.084)
503	2020-12-21	00:48:04.694 (0.480)	00:49:42.632 (0.590)	103.051 (1.212)

Table 2.1: Fitted times obtained for each light curve, [5]

The 3D shape of the moon was then projected to the occultation instant using the limb-fitting methodology already analyzed in the previous section. The chords for each occultation are then combined to fit the limb of the figure. The next image contains the chords and the fitted 3D limb. Regarding the 3D model used for all three moons are based on triaxial ellipsoids that represent the global shape of the satellites. This means that no topographic features were taken into account [5]. More specifically, the complex 3D shape of Io was taken from [25].

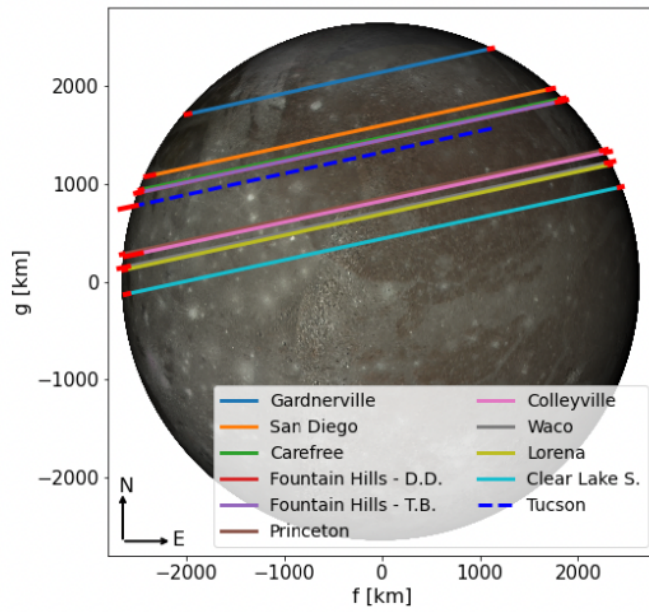


(a) Occultation by Io



(e) Occultation by 502 on 04/06/2019

(b) Occultation by Europa



(c) Occultation by Ganymede

Figure 2.2: Occultations by 501,502 and 503 taken from [5]

Finally, the new astrometric positions referenced to the geocenter obtained from the observational campaigns are organized in the following table, uncertainties in mas are given inside the brackets.

Body	Date and time UTC	Right ascension	Declination
501	2021-04-02 10:24	21h43m04s.37583 (1.1)	-14°23'58".1536 (0.7)
502	2019-06-04 02:26	17h16m59s.89400 (1.1)	-22°28'06".5375 (1.1)
503	2020-12-21 00:49	20h09m33s.56022 (0.9)	-20°35'38".0137 (1.7)

Table 2.2: Final astrometric positions [5]

Is interesting to compare the obtained positions at mas level with other geocentric ephemeris, in particular the De430 and jup365.

Body	RA (mas)	Dec (mas)	ΔRA_1	ΔDec_1	ΔRA_2	ΔDec_2
501	1.1	0.7	05.5	02.9	01.3	01.5
502	1.1	1.1	04.1	03.1	08.0	16.8
503	0.9	1.7	04.2	00.1	03.4	01.6

Table 2.3: Offsets in mas between the obtained positions and DE430 ($\Delta RA_1, \Delta Dec_1$) and jup365 ($\Delta RA_2, \Delta Dec_2$) [5]

3

VLBI

The VLBI spacecraft tracking technique has been successfully tested on numerous deep-space missions. Moreover, it imposes minimal requirements on the spacecrafts as it utilizes the same instruments used for communication, providing sufficient power and phase stability [26]. With the radio signals transmitted by the spacecraft's antenna, it is possible to determine its lateral position (the position in the two mutually orthogonal directions perpendicular to the line of sight vector) in the International Celestial Reference Frame (ICRF). These angular position measurements are obtained by means of Very Long Baseline Interferometry (VLBI), using many radio telescopes that observe at the same time the radio signal emitted by the spacecraft. Present state of the art measurements provide lateral position (right ascension and declination) observables with an uncertainty of 1 nrad or better in ICRF. VLBI measurements can be combined with the spacecraft orbit determination to provide accurate barycentric positions. These technique follows from [27], where barycentric positions in ICRF of Saturn have been successfully improved through phase-referenced very-long-baseline interferometry observations of Cassini combined with orbit determination from Doppler and range tracking. In this work, we assume to already have the post processed lateral measurements of the celestial bodies, but is good practice to have an overview of the overall processing from the signal to the final measurements. Let us dive into a deeper description on how VLBI spacecraft tracking works.

3.1 VLBI system

Let us consider a situation where the wavefront from a deep space radio source arrive as plane wave at two well separated antennas located on Earth. The signals are amplified and recorded. The recorded signals are then cross correlated to determine the difference in the time of arrival of the signal at the two stations as depicted in the following image.

This difference in time of arrival of the signal is referred to as the VLBI delay and is composed of a geometric delay and delays due to station clock offsets and differences in signal delays through the Earth's ionosphere and troposphere. The delay related to the geometry of the observation can

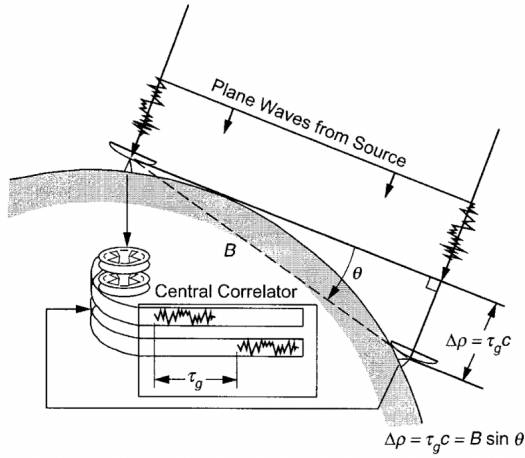


Figure 3.1: Geometry of observation, [28]

be expressed as follow:

$$\tau_g = \frac{1}{c} \mathbf{B} \cdot \hat{s} \quad (3.1)$$

Where \mathbf{B} is denoted as the baseline vector between two stations and \hat{s} is the unit vector in the source direction. With the a priori knowledge of the baseline length and orientation, it is possible to obtain from the geometric delay the angular component of the source position. The measurement of the angle formed by the radio signal and the baseline can be obtained.

$$\rho = c\tau_g = \mathbf{B} \sin(\theta) \quad (3.2)$$

Where θ in this case describes the angle misalignment between the baseline and the direction of the incoming signal. The accuracy to which the angle θ can be measured depends not only on the precision of the actual VLBI measurement but also on the measurement calibration (clock offsets, instrumental delays, baseline orientation errors).

3.1.1 Delta VLBI

A possible solution to effectively reduce calibration errors in VLBI measurements is to introduce a second measurement of a nearby source whose position is well known [28]. Using a second measurements can almost cancel entirely station clock offsets and instrumental delay. The nearby source acts as a calibrator and is called phase-reference calibrator. In phase referenced VLBI, alternated observations of the radio signal and the nearby calibrator are performed. Usually the radio source that acts as calibrator is a quasar. Over the last decades, a quasi inertial reference frame with an associated catalog of almost 200 source positions has been developed [29],[30]. Source positions are

determined in the international celestial reference frame (ICRF) with an uncertainties of better than 5 mrad [31].

The extent to which errors are eliminated in the differential observable depends greatly on how close the sources are, the time offset between observations and the similarity in spectral characteristics. For the case of two sources, where one is the spacecraft and the other one is a quasar, the spectral structure will be different. In fact, quasars have broadband signals while spacecraft signals are band limited and contain tones that are utilized for VLBI tracking. To solve this issue, open-loop recordings are made for each source using frequency channels centered at the spacecraft tone frequencies. The recorded data from all stations is then sent to a common JPL station. At this point, the quasar signal phase is extracted by cross correlation of the frequency channels between stations while the phase of each spacecraft tone is extracted by local model correlation.

The total delay is ambiguous to λn where n is an integer number of the radio frequency cycles and λ is the wavelength. Through bandwidth synthesis [32] is possible to determine the unambiguous delay. The unambiguous delay obtained from the spacecraft measurements is called differential one-way range (DOR) and the tones in the spacecraft spectrum are called DOR tones. Finally, the differential delay between spacecraft and quasar is referred to ΔDOR and gives a very accurate measure of the spacecraft angular position in the radio source reference frame

The most accurate measurement is obtained when both the target and the phase referencing calibrator are within the same primary beam of a VLBI antenna. The best switching time between the calibrator and the target ranges from tens of seconds to several minutes. Moreover, the ideal scan duration for each source depends on: the efficiency of the radio telescope, their system temperature and the slewing speed.

3.2 Sources of error

The main sources of error in a typical $\Delta VLBI$ observations are signal to noise ratios, uncalibrated troposphere and ionosphere delays, baseline errors and instrumental delays [28]. The magnitude of the errors depends highly on system parameters, for example, the signal to noise ratio for the extragalactic source depends on the quasar flux density, recording bandwidth and antenna parameters. Model for estimating the delays have been developed, here we highlight the delay model presented by Duev et al.,.

3.3 Delay Model

The VLBI delay model is expressed in the barycentric celestial reference system (BCRS), this requires several time-scale and station coordinates transformations. The first transformation to be applied to the station coordinates is a transformation from terrestrial reference system (ITRF) to geocentric celestial reference system (GCRS). This transformation is performed accordingly to the latest IERS

2010 conventions. Station positions and velocities in ITRF at epoch t_0 are reduced to the epoch of observation, taking into account the plate tectonic motion.

$$\mathbf{r}_{ITRF} = \mathbf{r}_0 + \dot{\mathbf{r}}_0(t - t_0) \quad (3.3)$$

Finally, station position, velocity and acceleration in GCRS are computed.

$$\mathbf{r}_{GCRS} = T(t) * \mathbf{r}_{ITRF}, (\mathbf{r}_{GCRS} \rightarrow \dot{\mathbf{r}}_{GCRS}, \ddot{\mathbf{r}}_{GCRS} \rightarrow \dot{T}(t), \ddot{T}(t)) \quad (3.4)$$

Where $T(t) = Q(t)R(t)W(t)$ where $Q(t), R(t), W(t)$ are matrices representing the motion of the celestial pole in GCRS rotation of the Earth around the axis associated with the pole and polar motion accordingly. Station positions are also corrected for geophysical effects.

Further, the geocentric to barycentric transformation is applied. The Lorentz transformation is applied to the station GCRS position, velocity and acceleration $(\mathbf{r}_{bc}, \dot{\mathbf{r}}_{bc}, \ddot{\mathbf{r}}_{bc})$ to transform it in solar system barycentric reference frame BCRS.

$$\begin{aligned} \mathbf{r}_{bc} &= \left(1 - L_C - \frac{\gamma U_E}{c^2}\right) \cdot \mathbf{r}_{gc} - \frac{1}{2c^2} (\mathbf{V}_E \cdot \mathbf{r}_{gc}) \cdot \mathbf{V}_E + \mathbf{R}_E \\ \dot{\mathbf{r}}_{bc} &= \left(1 - \frac{(1 + \gamma)U_E}{c^2} - \frac{V_E^2}{2c^2} - \frac{\mathbf{V}_E \cdot \dot{\mathbf{r}}_{gc}}{c^2}\right) \cdot \dot{\mathbf{r}}_{gc} \\ &\quad + \mathbf{V}_E \cdot \left(1 - \frac{1}{2c^2} (\mathbf{V}_E \cdot \dot{\mathbf{r}}_{gc})\right) \\ \ddot{\mathbf{r}}_{bc} &= \left(1 + L_C - \frac{(2 + \gamma)U_E}{c^2} - \frac{V_E^2}{c^2} - \frac{2\mathbf{V}_E \cdot \dot{\mathbf{r}}_{gc}}{c^2}\right) \cdot \ddot{\mathbf{r}}_{gc} \\ &\quad - \frac{1}{2c^2} (\mathbf{V}_E \cdot \ddot{\mathbf{r}}_{gc}) \cdot (\mathbf{V}_E + 2\dot{\mathbf{r}}_{gc}) + \mathbf{A}_E \end{aligned} \quad (3.5)$$

Where $L_C = 1.48082686741 \times 10^{-8}$ and $U_E = \sum_{j \neq i} \frac{GM_j}{r_{Ej}}$ is the potential of all solar system bodies except for the Earth, γ is the PPN parameter (equal to 1 in general relativity), $\mathbf{R}_E, \mathbf{V}_E, \mathbf{A}_E$ are position, velocity and acceleration of the Earth in BCRS and c is the speed of light.

The time-scale used for measurement timing is the coordinated universal time (UTC) which is different from the physically realised atomic time scale (TAI). The difference is by 34 leap-seconds. The latter, is different from the terrestrial time (TT) by 32.184 s. The terrestrial time is a scaled version of the geocentric coordinate time (TCG) and it eliminates the effect on the terrestrial clock by the gravitational potential from the Earth [33].

$$TCG = TT + L_G(JD_{TT} - TT_0) \quad (3.6)$$

Where TT_0 is the terrestrial time at 1977 January 1.

The time scale used in the ephemerides of a planetary spacecraft is the barycentric dynamical time (TDB) which is a scaled version of the barycentric coordinate time (TCB). The TDB stays

close to the terrestrial time ob average by applying the following transformation [33].

$$TDB = TCB - L_B(JD_{TCB} - T_0)86400 + TDB_0 \quad (3.7)$$

Where $T_0 = 2443144.5003725$, $L_B = 1.550519768 \times 10^{-8}$ and $TDB_0 = 6.44 \times 10^{-5} s$.

We can summarize the time-scale transformations as follows

$$UTC \rightarrow TAI \rightarrow TT \rightarrow TCG \rightarrow TCB \rightarrow TDB$$

3.3.1 VLBI delay model

The calculation of the VLBI signal delay follows from the consensus model recommended by IERS [26]. The model is based on plane-wave approximation by assuming the extragalactic source at infinite distance. The total geocentric vacuum delay is given by the following equation.

$$\begin{aligned} t_2 - t_1 = & \left(1 + \frac{\mathbf{K} \cdot (\mathbf{V}_E + \dot{\mathbf{r}}_{2,gc})}{c} \right)^{-1} \cdot \left(\Delta T_{grav} - \frac{\mathbf{K} \cdot \mathbf{b}}{c} \right. \\ & \cdot \left[1 - \frac{(1 + \gamma)U_E}{c^2} - \frac{\mathbf{V}_E^2}{2c^2} - \frac{\mathbf{V}_E \cdot \dot{\mathbf{r}}_{2,gc}}{c^2} \right] \\ & \left. - \frac{\mathbf{V}_E \cdot \mathbf{b}}{c^2} \cdot \left(1 + \frac{\mathbf{K} \cdot \mathbf{V}_E}{2c} \right) \right). \end{aligned} \quad (3.8)$$

Where \mathbf{K} is the unit vector from the barycentre to the source in the absence of bending and \mathbf{b} is the GCRS baseline vector at the time of signal arrival at the first station. δT_{grav} is the general relativistic delay. The total gravitational delay is given as the sum over all gravitating bodies including Earth.

The delay model for spacecraft VLBI observations accounts for the near-field effects caused by the source being at finite distance [26]. The diffracted radio wave is considered to be in the near-field when the distance R to the source from the aperture is $R \leq \frac{D^2}{\lambda}$ [34]. Where D is the characteristics size of the aperture and λ is the wavelength. In the TDB reference frame, the signal delay is defined as the time difference between two light travel times LT_1, LT_2 from the spacecraft from the first and the second station along the baseline. The geometry in the barycentric celestial reference frame can be visualised in the following image.

Given the reception time T_1 in TBD at the first station, the transmission time T_0 is calculated iteratively solving the light-time equation for 0-1.

$$T_1 - T_0 = \frac{R_{01}}{c} + RLT_{01} \quad (3.9)$$

Where RLT_{01} is a relativistic term which takes into account effects for both general and special relativity [35]. Given the solution T_0 , the light-time equation for 0-2 is solved for T_2 using the same methodology. The difference $T_2 - T_1$ is the VLBI delay in the barycentric TDB frame, which is then

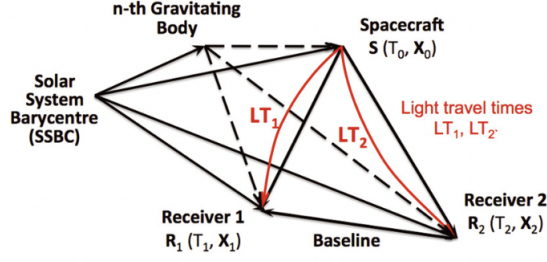


Figure 3.2: VLBI geometry, [26]

transformed into the geocentric TT frame.

Other sources that have impact on the signal delay are random fluctuations in the radio wave phase which are caused by interplanetary scintillations in the solar wind [26]. Moreover, the Earth's ionosphere and troposphere also induce additional delay to the radio signal propagation. To mitigate the effects of the latter, vertical total electron content (vTEC) provided by international GNSS service are used. The vTEC must be mapped onto the direction of the target source to obtain the slant total electron content (TEC).

$$TEC = \frac{vTEC}{\cos z'} \quad (3.10)$$

Where z^1 is the zenith distance of the target as seen from the model's ionospheric layer. The ionospheric delay for each station can be computed.

$$\tau_{iono} = \frac{5.308018TEC}{4\pi^2 f^2} \quad (3.11)$$

Where f is the observational frequency.

3.3.2 Estimation of spacecraft state vector

The main task of VLBI tracking of spacecraft is to estimate its state vector as a function of time. The measurement equation for each epoch t is given by:

$$\overrightarrow{\Delta\phi}\Big|_t = \left(J_{ij} \cdot \overrightarrow{\Delta\alpha} \right)\Big|_t \quad (3.12)$$

Where $\overrightarrow{\Delta\phi}$ is a vector of differential phases on all baselines and $\overrightarrow{\Delta\alpha}$ is the vector of corrections to the a priori geocentric angular position of the spacecraft. J_{ij} is the Jacobian of partial derivatives of the geocentric delay for station i at time t with respect to the geocentric spherical angular coordinates of the source (ϕ, θ) .

$$\overrightarrow{\Delta\phi} = \begin{pmatrix} \phi_{12} \\ \vdots \\ \phi_{1N} \\ \vdots \\ \phi_{N-1,N} \end{pmatrix}, \overrightarrow{\Delta\alpha} = \begin{pmatrix} \Delta\varphi \\ \Delta\theta \end{pmatrix} \quad (3.13)$$

Finally, the astrometric solution to 3.12 in the least-squares sense for each epoch is given by

$$\overrightarrow{\Delta\alpha}\Big|_t = \left((J^T \cdot J)^{-1} \cdot J^T \cdot \overrightarrow{\Delta\phi} \right)\Big|_t \quad (3.14)$$

3.4 Improvements of Jupiter ephemeris using VLBA astrometry of spacecraft

The Very Long Baseline Array (VLBA) consists of 10 radio telescopes which are part of the National Radio Astronomy Observatory (NRAO) [36]. This system is the longest system in the world that uses very long baseline interferometry with a baseline of 8611 km. VLBA has been used since August 2016 to make phase-referenced astrometric measurements of JUNO spacecraft (NASA) which is in orbit around Jupiter [37]. These astrometric measurements are then combined with solutions for JUNO's orbit to provide accurate positions for the Jupiter system barycenter in the international celestial reference frame (ICRF). The major sources of errors are ionosphere and troposphere calibration, spacecraft orbit determination and phase reference position uncertainties. The VLBA are scheduled when JUNO passes at the pericenter of its orbit that is at 4200km from Jupiter, when the spacecraft Doppler signature is largest, this provides the strongest orbit constraints. The rms ($1 - \sigma$) uncertainties in the Jupiter barycentric positions are estimated to be 0.2-0.3 mas in right ascension and 0.3-0.4 mas in declination. The results of these observations will improve Jupiter's orbit in the Jet Propulsion Laboratory (JPL) planetary ephemeris.

4

State Estimation

In the real world, it is impossible to have perfect measurements and perfect dynamical models, therefore estimation is required. Errors arise from many sources and they are usually mitigated by observations through orbit determination. The main sources of error are the instrument and measurement error.

Instrument error arise from sensor maintenance, operator error and so forth. These factors can easily corrupt the data. The measurement error, can be defined as the variation in the observations from their true value. It can be divided in three main categories: noise, biases and non-random time-varying errors also known as drift [38].

We can define the bias as a constant offset from the true value. The noise is a statistical measure, the standard deviation, of the random variation about the measured mean value. Finally, the drift represent a slow and especially unpredictable variation of the observed mean value over a time span. Usually biases cannot be removed with least-squares techniques but measurement biases can be estimated during the estimation.

Before diving into the estimation techniques, it is necessary to introduce some statistical concepts that will be used heavily in the following chapter.

We first introduce the concept of probability of an event $\xi < x < \xi + d\xi$ for a random variable x is $p(\xi)d\xi$. The probability distribution is subject to the condition that the integral over all possible values is equal to one [38].

$$\int_{-\infty}^{\infty} p(\xi)d\xi = 1 \quad (4.1)$$

We define the mean as \bar{x} , and is the expected value of an event occurring over all possibilities. Moreover, we define the sample mean which contains only a subset of the possible outcomes. The averages for a finite sample for large N , approximates the corresponding integral expectations.

$$\bar{x} \equiv E(x) = \int_{-\infty}^{\infty} p(\xi)d\xi \cong \frac{1}{N} \sum_{i=1}^N \xi_i \quad (4.2)$$

The *Law of large numbers* permits to approximate \bar{x} using the sample mean. This approximation is the fundamental basis for Monte-Carlo methods. As the size of the sample grows, the distribution becomes Gaussian.

We can also define the root mean square (RMS) which is the square root of the mean expected squared value.

$$RMS = \sqrt{E(x^2)} \cong \sqrt{\frac{1}{N} \sum_{i=1}^N \xi_i^2} \quad (4.3)$$

The sample variance, σ^2 represents the variability of the expected value of each variable about the sample mean:

$$\sigma^2 \equiv E[(x - E[x])^2] = E[(x - \bar{x})^2] = \int_{-\infty}^{\infty} (\xi - \bar{x})^2 p(\xi) d\xi \cong \frac{1}{N-1} \sum_{i=1}^N (\xi_i - \bar{x})^2 \quad (4.4)$$

From the sample variance we can define the sample standard deviation, σ , which is the positive square root of the variance. The standard deviation measures the dispersion of the data. Is important to note that the RMS and the standard deviation are usually not the same, they are the same only when the mean is zero.

The likelihood of an occurring event is described by $p(\xi)$, probability density function. For a Gaussian random variable, we can define its PDF as:

$$p(\xi) = \frac{1}{\sqrt{2\pi}\sigma} e^{-\frac{(\xi-\bar{x})^2}{2\sigma^2}} \quad (4.5)$$

The following image shows a Gaussian probability density function.

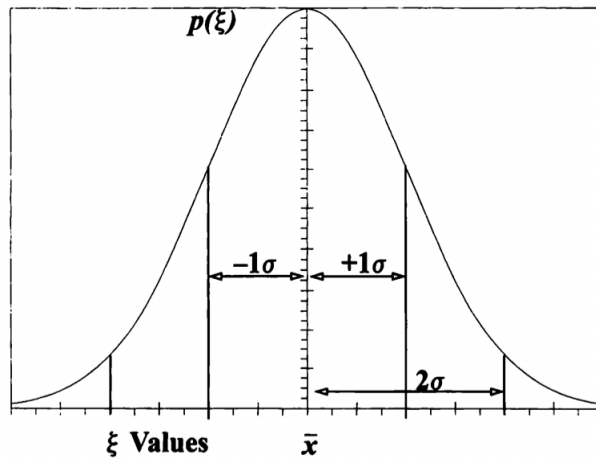


Figure 4.1: Gaussian distribution, [38]

4.1 Linear Weighted Least squares

The linear weighted least squares method introduces weights in order to account for differences in the accuracy of the measurements. Suppose that an estimate of the true state vector of an object is known. We define the estimate as $\hat{\mathbf{x}}$ and the true state vector as $\mathbf{x} = [\mathbf{r}_0, \mathbf{v}_0]$ at a certain epoch t_0 . We define $\mathbf{r}_0, \mathbf{v}_0$ as the position and velocity components at t_0 . Our goal is to refine the estimate exploiting observations which are made by a number of p lateral position measurements at several time instants $t_i, i = 1, 2, \dots, p$. With numerical integration it is possible to propagate the first guess up to t_p , predict the lateral measurements and measurement times and compute the difference with the actual true observations. We call this difference as *residual*. We define the vector of actual observations \mathbf{z} and the vector of computed observations $\hat{\mathbf{z}}$ which is a function of $\hat{\mathbf{x}}$. The goal is to find $\hat{\mathbf{z}}$ that minimizes a cost function J , which is defined as the weighted average of the norm of the residuals.

$$J(\hat{\mathbf{x}}) = [\mathbf{z} - \hat{\mathbf{z}}(\hat{\mathbf{x}})]^T \mathbf{W} [\mathbf{z} - \hat{\mathbf{z}}(\hat{\mathbf{x}})] \quad (4.6)$$

Where W is a $p \times p$ square matrix denoted as the weight matrix, and is taken as the inverse of the measurement noise covariance matrix [39]. The weight matrix is used not only to weight individual observations, but also to weight classes of observation which are assumed to have similar characteristics. The inverse is used so that a small value (in other words, a more accurate observation) will weight the sensor more than a larger value [38]. The weight matrix is defined as follow:

$$\mathbf{W} = w_i^T w_i = \begin{bmatrix} w_1^2 & 0 & \dots & 0 \\ 0 & w_2^2 & & \\ \vdots & & & \vdots \\ 0 & \dots & 0 & w_N^2 \end{bmatrix} \quad (4.7)$$

Where

$$w_i = \begin{bmatrix} \frac{1}{\sigma_A} & 0 \\ 0 & \frac{1}{\sigma_B} \end{bmatrix} = \begin{bmatrix} w_A & 0 \\ 0 & w_B \end{bmatrix} \quad i = 1 \dots p \quad (4.8)$$

w_A and w_B are the inverses of the standard deviations associated with the set of observations A and B. This is done in such a way to minimize the trace of the error covariance matrix \mathbf{P} .

If the cost function J is at a minimum, then we can say

$$\frac{\partial J}{\partial \hat{\mathbf{x}}} = \left[\frac{\partial J}{\partial \hat{r}_1} \quad \frac{\partial J}{\partial \hat{r}_2} \quad \frac{\partial J}{\partial \hat{r}_3} \quad \frac{\partial J}{\partial \hat{v}_1} \quad \frac{\partial J}{\partial \hat{v}_2} \quad \frac{\partial J}{\partial \hat{v}_3} \right] = 0 \quad (4.9)$$

Which, from equation 4.6 yields the result

$$\frac{\partial J}{\partial \hat{\mathbf{x}}} = -2(\mathbf{z} - \hat{\mathbf{z}})^T \mathbf{W} \frac{\partial \hat{\mathbf{z}}}{\partial \hat{\mathbf{x}}} = 0 \quad (4.10)$$

In which in our case, the partial derivatives of $\hat{\mathbf{z}}$ with respect to $\hat{\mathbf{x}}$ are the partial derivatives of the right ascension and declination with respect to the components of the moon position and velocity at t_0 . These partials are grouped in a $p \times n$ matrix denoted as *design matrix* $H(t)$. The design matrix has the following shape:

$$\mathbf{H}(\mathbf{t}) = \frac{\partial \hat{\mathbf{z}}(t)}{\partial \hat{\mathbf{x}}} \quad (4.11)$$

Where $\hat{\mathbf{z}}$ is the vector containing of computed observations and $\hat{\mathbf{x}}$ is the vector of all estimated parameters $[\mathbf{x}_0; \mathbf{p}]$. The derivatives are numerically approximated through finite difference. Since the dependence of J on the estimated parameters is non linear, the solution to the minimization problem can be given using iterative corrections methods, e.g., Newton-Raphson methods. If we take the transpose of 4.10, then the estimate $\hat{\mathbf{x}}$ must satisfy:

$$\mathbf{H}^T \mathbf{W}(\mathbf{z} - \hat{\mathbf{z}}) := G(\hat{\mathbf{x}}) = 0 \quad (4.12)$$

The differential correction between the iterations $n + 1$ and n is computed as follow:

$$\hat{\mathbf{x}}^{(n+1)} - \hat{\mathbf{x}}^{(n)} = -G' [\hat{\mathbf{x}}^{(n)}]^{-1} G [\hat{\mathbf{x}}^{(n)}] = \left(\mathbf{H}^T \mathbf{W} \mathbf{H} \right)^{-1} \mathbf{H}^T \mathbf{W} [\mathbf{z} - \hat{\mathbf{z}}(\hat{\mathbf{x}}^{(n)})] \quad (4.13)$$

Where the gradient G is computed by assuming the design matrix to be independent on \mathbf{x} . Using the estimate at $n + 1$ is possible to compute a new trajectory and new residuals. The process is repeated until the residuals cease to become smaller with further iterations. The error of the converged estimate, defined as $\delta \mathbf{x} = \mathbf{x} - \hat{\mathbf{x}}$ can be evaluated by computing the error covariance matrix $P = E[\delta \mathbf{x} \delta \mathbf{x}^T]$, where E is the average. The resulting error $\delta \mathbf{x}$ is related to the converged residual vector $\delta \mathbf{z} = \mathbf{z} - \hat{\mathbf{z}}$ by 4.13 . We assume it has covariance equal to the inverse of the weight matrix:

$$E[\delta \mathbf{z} \delta \mathbf{z}^T] = \mathbf{W}^{-1} \quad (4.14)$$

By multiplying eq 4.13 by its transpose and averaging, we finally get the covariance matrix.

$$\mathbf{P} = \left(\mathbf{H}^T \mathbf{W} \mathbf{H} \right)^{-1} \quad (4.15)$$

The covariance matrix contains the estimates for the closeness of the fit with the chosen dynamics and it contains both variances and covariances. If we assume an unitary weight matrix, the covariance matrix has the following general shape:

$$\mathbf{P} = \begin{bmatrix} \sigma_\alpha^2 & \mu_{\alpha\beta} \sigma_\alpha \sigma_\beta & \cdots \\ \mu_{\beta\alpha} \sigma_\alpha \sigma_\beta & \sigma_\beta^2 & \cdots \\ \vdots & \vdots & \ddots \end{bmatrix} \quad (4.16)$$

Where σ_α is the standard deviation of the estimated parameter, σ_α^2 is the variance and $\mu_{\beta\alpha}$ is the correlation coefficient of α and β . They are defined as $\mu_{xy}^2 = (1/\sigma_x\sigma_y)E[(\mathbf{x} - \bar{\mathbf{x}})(\mathbf{y} - \bar{\mathbf{y}})]$. These coefficient represent the degree of correlation between elements, with zero being uncorrelated. Positive signs represent a direct correlation while negative signs imply an inverse relationship.

With this shape, the main diagonal of the covariance matrix represents the variances of the estimate of the state parameters. Therefore, the main diagonal is correlated to the formal uncertainty σ of the corresponding element of the state vector through the relation

$$\sqrt{P_{ii}} = \sigma_i \quad (4.17)$$

In our case, the covariance matrix will have the initial states of the bodies. Moreover, an additional *a priori covariance* is used in the inversion. The a priori covariance contains the current knowledge of the parameters. The final shape of the covariance matrix is:

$$\mathbf{P} = (\mathbf{P}_0^{-1} + \mathbf{H}^T \mathbf{W} \mathbf{H})^{-1} \quad (4.18)$$

4.1.1 Variational Equations formulation

The variational equations describe how the dynamics of the system are influenced by the parameters to be estimated. We denote the state vector \mathbf{x} that is propagated numerically from the initial time t_0 following [40]:

$$\dot{\mathbf{x}}(t) = \mathbf{f}(\mathbf{x}, \mathbf{p}, t); \mathbf{x}(t_0) = \mathbf{x}_0 \quad (4.19)$$

Where \mathbf{p} , is, as previously mentioned, a vector of parameters that influence the system's dynamics and \mathbf{f} is the used dynamical model and \mathbf{x}_0 is the associated initial condition. As mentioned in the above chapter, we defined \mathbf{H} as the matrix of the observations at different times with respect to the state vector at t_0 . From this statement, we can observe that the design matrix describes how changes in the initial state affect the computed observations. These are usually called sensitivity partial derivatives. We can break down the design matrix the following way [38]:

$$\mathbf{H} = \frac{\partial \hat{\mathbf{z}}}{\partial \hat{\mathbf{x}}_0} = \frac{\partial \hat{\mathbf{z}}}{\partial \hat{\mathbf{x}}} \frac{\partial \hat{\mathbf{x}}}{\partial \hat{\mathbf{x}}_0} = \mathbf{H} \Phi(t, t_0) \quad (4.20)$$

The equation 4.20 makes the distinction between the observation partial derivatives \mathbf{H} and the derivative of the state over time. Φ is called *state transition matrix* and it relates the state errors at t with the state errors at time t_0 . The two matrices in Φ are calculated by means of numerical integration or by finite difference. We can describe the influence of a change in initial conditions \mathbf{x}_0 and/or \mathbf{p} on the resulting state history $\mathbf{x}(t)$ by making a linear approximation¹:

$$\Delta \mathbf{x}(t) \simeq \frac{\partial \mathbf{x}(t)}{\partial \mathbf{x}_0} \Delta \mathbf{x}_0 + \frac{\partial \mathbf{x}(t)}{\partial \mathbf{p}} \Delta \mathbf{p} \quad (4.21)$$

¹Tudat mathematical model definition

Where we can identify the first partial as the state transition matrix Φ . Moreover, we can define the second partial as the *sensitivity matrix*:

$$\mathbf{S}(t) = \frac{\partial \mathbf{x}(t)}{\partial \mathbf{p}} \quad (4.22)$$

The differential equations used to solve for Φ, \mathbf{S} are termed the variational equations [41] and are obtained by numerical integration [42]:

$$\begin{aligned} \frac{d\Phi(t, t_0)}{dt} &= \frac{\partial \dot{\mathbf{x}}}{\partial \mathbf{x}} \frac{\partial \mathbf{x}}{\partial \mathbf{x}_0} \\ &= \left(\frac{\partial \mathbf{f}}{\partial \mathbf{x}} \right) \Phi(t, t_0) \\ \frac{d\mathbf{S}(t)}{dt} &= \frac{\partial \dot{\mathbf{x}}}{\partial \mathbf{x}} \frac{\partial \mathbf{x}}{\partial \mathbf{p}} + \frac{\partial \dot{\mathbf{x}}}{\partial \mathbf{p}} \\ &= \left(\frac{\partial \mathbf{f}}{\partial \mathbf{x}} \right) \mathbf{S}(t) + \frac{\partial \mathbf{f}}{\partial \mathbf{p}} \end{aligned} \quad (4.23)$$

With the following initial conditions:

$$\Phi(t_0, t_0) = \mathbf{1}_{n \times n}; \mathbf{S}(t_0) = \mathbf{0}_{n \times n_p}$$

where (n, n_p) are the sizes of the state vector \mathbf{x} and parameter vector \mathbf{p} . In this work, the variational equations involve the situation where the vector \mathbf{x} represents the translational state of one or more moon. For a single moon's translational dynamics, we obtain:

$$\mathbf{x} = \begin{pmatrix} \mathbf{r} \\ \mathbf{v} \end{pmatrix}; \mathbf{f} = \begin{pmatrix} \mathbf{v} \\ \mathbf{a} \end{pmatrix} \quad (4.24)$$

From here, we obtain the partial derivatives in the variational equations as:

$$\frac{\partial \mathbf{f}}{\partial \mathbf{x}} = \begin{pmatrix} \mathbf{0}_{3 \times 3} & \mathbf{1}_{3 \times 3} \\ \frac{\partial \mathbf{a}}{\partial \mathbf{r}} & \frac{\partial \mathbf{a}}{\partial \mathbf{v}} \end{pmatrix}; \frac{\partial \mathbf{f}}{\partial \mathbf{p}} = \begin{pmatrix} \mathbf{0}_{3 \times n_p} \\ \frac{\partial \mathbf{a}}{\partial \mathbf{p}} \end{pmatrix} \quad (4.25)$$

Where the argument t has been omitted for clarity.

4.2 Propagation of the covariance matrix

We have seen that the covariance matrix is used to evaluate an estimated solution. Here, we want to know how good is the estimate in the future. This is done by propagating the covariance matrix along with the state propagation. The covariance matrix will give a first indication of the accuracy of the solution at each epoch. Over time, the error will eventually grow. We recall the design matrix as the matrix of partial derivatives of the observations up to time T with respect to the estimated

parameters.

$$\mathbf{H}(T) = \frac{\partial \mathbf{h}(T)}{\partial \mathbf{q}}, \mathbf{q} = [\mathbf{x}_0; \mathbf{p}] \quad (4.26)$$

We define \mathbf{q} as the vector containing all estimated parameters [40],[43] and $x\mathbf{x}_0, \mathbf{p}$ as the initial state vector and a vector of parameters that influence the system dynamics. We then define the covariance matrix of \mathbf{q} obtained using the data up to the time T as:

$$\mathbf{P}_{\mathbf{q}\mathbf{q}}(T) = (\mathbf{P}_{\mathbf{q}\mathbf{q},0}^{-1} + \mathbf{H}^T(T)\mathbf{W}(T)\mathbf{H}(T))^{-1} \quad (4.27)$$

where $\mathbf{P}_{\mathbf{q}\mathbf{q},0}$ is the a priori covariance matrix of the parameters \mathbf{q} and $\mathbf{W}(T)$ is the weight matrix. The covariance matrix obtained can be used to compute the covariance of the state \mathbf{x} at any later time t [41]. This propagated covariance can be defined as:

$$\mathbf{P}_{xx}(t, T) = [\Phi(t, t_0); \mathbf{S}(t)]\mathbf{P}_{\mathbf{q}\mathbf{q}}(T)[\Phi(t, t_0); \mathbf{S}(t)]^T \quad (4.28)$$

Where the state transition matrix Φ and sensitivity matrix \mathbf{S} are computed using equation 4.23. The formal uncertainties are obtain again as the square root of the main diagonal of \mathbf{P} .

4.2.1 Covariance Matrix transformation

The covariance matrix is usually expressed in the inertial reference frame. The transformation relies on the similarity transformation [38]

$$\mathbf{P}_y = m\mathbf{P}_x m^T, m_{\frac{y}{x}} = \frac{\partial y}{\partial x} \quad (4.29)$$

Where m is the Jacobian of the transformation. In this study, we will express the propagated uncertainties in the RSW orientation where R is radial, S is along track and W is cross track direction respectively. To change the orientation from inertial coordinates to RSW orientation we use the following transformation.

$$[J] = \begin{bmatrix} [\hat{R}|\hat{S}|\hat{W}]^T & [0] \\ [0] & [\hat{R}|\hat{S}|\hat{W}]^T \end{bmatrix}; \mathbf{P}_{RSW} = [J]\mathbf{P}_{xyz}[J]^T \quad (4.30)$$

We can visualize the orientation of the RSW reference frame in the next illustration.

Propagation of uncertainties in terms of lateral position

Since the two classes of observations performed in this work give lateral positions measurements, that are right ascension α and declination δ it is convenient to express the formal uncertainties in (α, δ) instead of RSW or in cartesian coordinates.

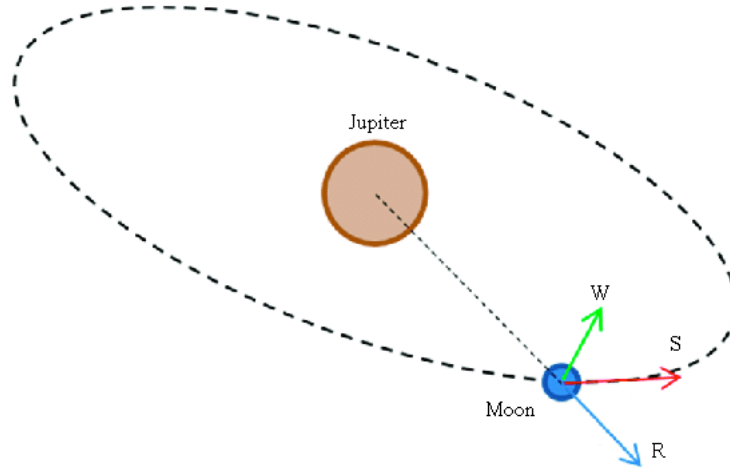


Figure 4.2: RSW reference frame

Right ascension, declination and geocentric distance r is a way to express the position of a body in the geocentric equatorial reference frame (J2000). The right ascension $\alpha \in [0^\circ, 360^\circ]$ is the angle measured eastward in the equatorial plane, between the x axis and a plane which is normal to the equator (meridian plane) and containing the body. The declination $\delta \in [-90^\circ, 90^\circ]$ is the angle between the equatorial plane and the geocentric radius vector defining the position of the body and it is measured in the meridian plane containing the body. The following image illustrates the coordinates in the geocentric equatorial reference system.

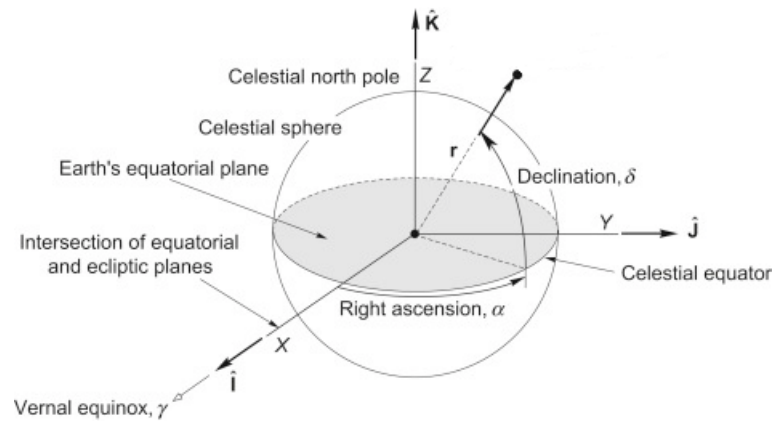


Figure 4.3: Geocentric equatorial reference system, [44]

To transform the cartesian coordinates from the inertial reference frame to right ascension and declination we use the notation from [45]. First, we derive the partial derivatives of α, δ with respect to the vector $\mathbf{r}(t) = [x, y, z]$ containing the position of the target moon with respect to the observer,

which in this case is Earth and $r = \text{norm}(\mathbf{r})$.

$$\frac{\partial \alpha}{\partial \mathbf{r}} = \frac{1}{x^2 + y^2} \begin{bmatrix} -y & x & 0 \end{bmatrix}^T \quad (4.31)$$

$$\frac{\partial \delta}{\partial \mathbf{r}} = \frac{1}{r^2 + \sqrt{x^2 + y^2}} \begin{bmatrix} -xz & -yz & x^2 + y^2 \end{bmatrix}^T \quad (4.32)$$

We can then create the transformation matrix \mathbf{J} which is 2×3 , containing the partials derivatives calculated above:

$$\mathbf{J} = \begin{bmatrix} \frac{\partial \alpha}{\partial \mathbf{r}} \\ \frac{\partial \delta}{\partial \mathbf{r}} \end{bmatrix} \quad (4.33)$$

We then apply the transformation matrix to the covariance matrix to be propagated where \mathbf{P}_x and \mathbf{P}_y are the covariance matrices expressed in (x, y, z) and (α, δ) respectively:

$$\mathbf{P}_y = \mathbf{J} \mathbf{P}_x \mathbf{J}^T \quad (4.34)$$

Where \mathbf{P}_y is a 2×2 matrix containing the variances and covariances expressed in terms of right ascension and declination at each time step t . The formal errors at each epoch can be extracted by taking the square root of the elements on the main diagonal.

5

Dynamical Model

This chapter describes the dynamical model used in the simulations. All the methods previously described are implemented using the TU Delft Astrodynamics Toolbox (Tudat) software¹. The software is freely available. Since in this work we are focused on analyzing the effect of Jupiter's uncertainties on the Moons formal errors, we decouple the orbit determination of the spacecraft from the ephemeris generation. In this chapter, we outline the state nomenclature and relative geometry, the data type and quality used in the simulations and the model used to simulate the observations.

5.1 States Formulation and Geometry

All the propagated states are expressed in an inertial reference frame with inertial orientation J2000. The J2000 orientation is defined in Tudat as a right-handed inertial frame which has the x axis towards vernal equinox, and the z axis aligned with Earth's rotation axis as it was at the J2000 epoch (1st of January 2000). We now indicate the translational state of body B, expressed in a frame with origin at the barycenter of body A, is denoted as $\mathbf{x}_B^{(A)}$. For simplicity, we denote the inertial frame origin SSB (Solar System Barycenter) by I . Following this notation, we obtain:

$$\mathbf{x}_B^{(I)} = \mathbf{x}_B^{(A)} + \mathbf{x}_A^{(I)} \quad (5.1)$$

This clearly implies that any derivative of the inertial state of the body B is obtained as:

$$\frac{\partial \mathbf{x}_B^{(I)}}{\partial x} = \frac{\partial \mathbf{x}_B^{(A)}}{\partial * } + \frac{\partial \mathbf{x}_A^{(I)}}{\partial * } \quad (5.2)$$

For the specific case of this analysis, the state vector is defined as:

$$\mathbf{x}(t) = \begin{pmatrix} \mathbf{x}_J^I(t) \\ \mathbf{x}_i^J(t) \end{pmatrix}; i = 1 \dots 2 \quad (5.3)$$

Where the letter J refers to Jupiter and the indices 1,2 refer to Io and Callisto respectively.

¹Documentation: <https://tudat-space.readthedocs.io>

Following this nomenclature the final position of the i -th moon in the inertial reference frame will be given by:

$$\mathbf{x}_i^{(I)} = \mathbf{x}_i^{(J)} + \mathbf{x}_J^{(I)}; i = 1 \dots 2 \quad (5.4)$$

It is important to note that in Tudat, since the global frame origin is the SSB, when calculating the dynamics of the moon w.r.t. Jupiter, the relative position of the moon w.r.t. Jupiter is calculated by subtracting the barycentric positions of the i -th moon and Jupiter to compute the relative position. Further, it is possible to visualize the general geometry that is being simulated by looking at the following image:

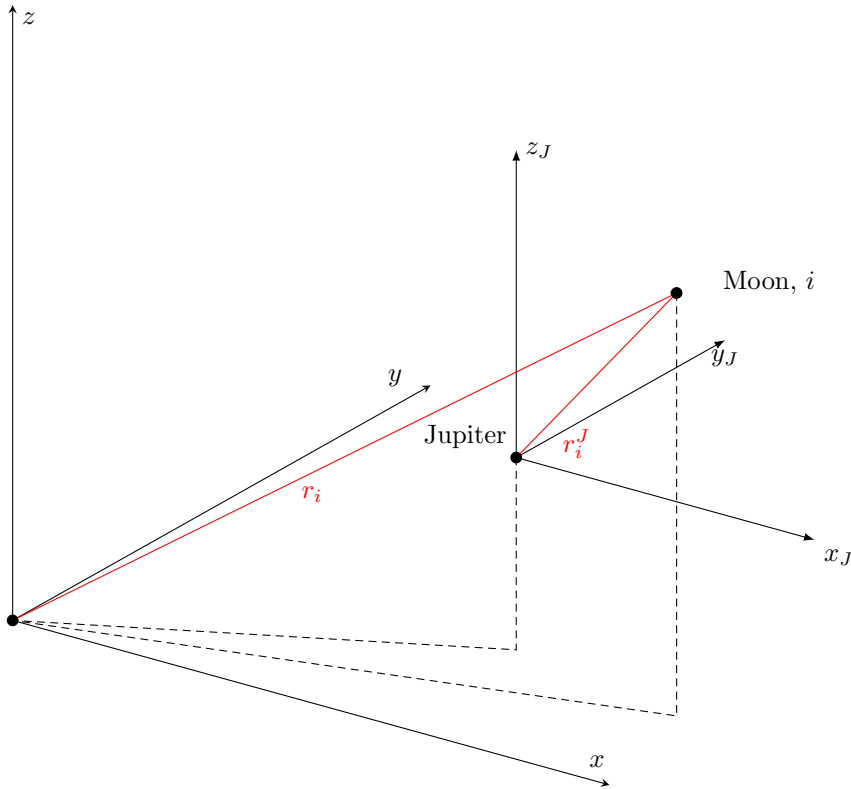


Figure 5.1: General geometry of the observation where the origin corresponds to Earth. The vector r_i corresponds to the position of the i -th moon with respect to Earth while the vector r_i^J expresses the position of the moon with respect to the barycenter of Jupiter.

5.2 Data type

The data used in this work is VLBI spacecraft tracking measurements and stellar occultation measurements. Both observable types provide lateral position measurements expressed in terms of right ascension and declination (α, δ) . The VLBI tracking provides the lateral position of the spacecraft

at a specific time in the international celestial reference frame (ICRF). Once the solution for the orbit of the spacecraft with respect to Jupiter is known through doppler tracking, it is possible to obtain the position of Jupiter with respect to the solar system. In this work we will not perform the orbit determination of the spacecraft and we will only consider the post-processed lateral positions of Jupiter. To summarize, the data types used in the simulations are:

- Lateral positions (VLBI) observed from Earth, of the Jupiter barycenter with respect to ICRF $(\alpha_J, \delta_J)^{ICRF}$
- Optical astrometry (stellar occultation) of the moon i from Earth-based observatories (α_i, δ_i) referenced to the Earth barycenter

5.2.1 Data quality and weights

In this section we define the quality of the data that are used as input to the covariance analysis, as well as the associated observation weights. The VLBI data uncertainty is expected to be at the level of 0.5 nrad for both right ascension α and declination δ . It is important to point out that current systems use an X-band signal, while for JUICE mission both a Ka- and Ka-band signal will be available. The use of such high frequency signals, which have a wavelength that is almost 4 times shorter than X-band, could result in observables that are almost 3-4 times more precise [46] [47]. Regarding Earth based optical astrometry such as stellar occultations measurements, the uncertainty used in this work is 1 mas based on the latest positions obtained in [5], that is equivalent to 4.84 nrad. To account for systematic errors, the VLBI measurements include an arc-wise bias of 0.5 nrad in both right ascension and declination. It is important to note that usually the VLBI uncertainty is applied to the spacecraft and not to the planet. To account for this, we assume that the orbit determination accuracy of the spacecraft with respect to Jupiter is much smaller compared to the accuracy of the actual VLBI observation referenced to the spacecraft. We do this by considering only one observable exactly at the time of the perijove of the spacecraft, which is about at a radial distance of 4,300 km from its surface. This allows to translate the uncertainty from the spacecraft to Jupiter's center of mass. About the stellar occultation, the final astrometric position has 4 main sources: the star, the ephemeris, the fitted shape and the reduction process. Therefore there are four main sources of bias. The Gaia EDR3 has a bias in proper motion that is already handled by SORA. Moreover, the fitted shape can be biased. Usually an ellipsoidal shape is used to fit the chords at the center of figure. However, for small bodies the elliptical shape may be wrong, thus creating a bias in the final position. Bias can also be generated in the reduction process, for example due to solar light deflection in the relative position of the star and the body. Many other sources of bias can be identified: if the occulted star is a single star or a binary star, in the fitting process the center of figure may differ from the center of mass and timing delays in the observations. As a conservative estimate, we applied a bias with an a priori constraint set to 4 mas (1.94 nrad) in both right ascension and declination.

5.3 Moon uncertainty simulation

In this section we highlight the methodology that we took to simulate the and propagate the uncertainty of the ephemerides of the Galilean moons starting from stellar occultation and VLBI data. We will discuss the parameters that we will consider in the simulations and the use of covariance analysis which has been discussed in great details in section 4.2. Moreover, we will also discuss some mitigation strategies that have been used to reduce the high condition number in the estimation problem. It is important to point out at this stage that realistically propagating the ephemeris uncertainties over a long time period is beyond the scope of this analysis as it would require adding additional data sets of current and upcoming missions like Juno, JUICE, Europa Clipper *etc.* [3].

5.3.1 Estimated parameters

In this work we estimate the initial state of the moon in a Jupiter-centered reference frame and the initial state of Jupiter in a barycentric reference frame with inertial orientation. In order to mitigate systematic errors in the measurements [3], we estimate also an arcwise bias in both right ascension and declination for each of the two data types.

5.3.2 Covariance analysis

We use the simulated observations of stellar occultation and VLBI as input to a covariance analysis, as described in the section 4.2 as done by. We know that usually the formal errors obtained with this type of technique are too optimistic [3]. However it is sufficient for this work as we are mainly interested in the contribution of VLBI data to the stellar occultation. The error between the true and formal errors is usually hard to quantify as it originates from non-white measurement noise, as well as inaccuracies in the planetary system's dynamics. Typically planetary ephemeris have a true-to-formal ratio of 2-3 [48]. The use of covariance analysis in the preliminary steps of a mission design has been conducted for a large variety of previous, current and upcoming missions [49][50][51][52] with a focus on many different types of data. Usually such studies have been on the direct science return of spacecraft tracking (gravity fields and others physical parameters)[3] whereas this work will primarily focus on the analysis of the dynamics of the natural satellites of Jupiter. Covariance analysis provide more realistic results when analyzing the estimation of natural bodies, compared to orbiter dynamics as the dynamical model used are able to capture the full observable behaviour [2]. On the other hand, for orbiter dynamics simulation and estimation, the dynamical model errors are not captured by a covariance analysis. This causes the true-to-formal error ratios of estimated parameters from spacecraft tracking to be in the order of 10 [53][52]. We computed the covariance for different scenarios where only stellar occultation and the combination of stellar occultation plus VLBI are performed. The different scenarios will be analyzed further for each moon.

5.3.3 A priori knowledge

As already described in 4, a prior knowledge of the states is taken into consideration in the estimation by means of the a priori covariance matrix \mathbf{P}_0 . Appropriate values for the a priori knowledge for the estimated parameters are further discussed. The general shape of the a priori covariance matrix is the following:

$$\mathbf{P}_0 = \begin{bmatrix} \mathbf{P}_{0,i} & 0 \\ 0 & \mathbf{P}_{0,J} \end{bmatrix} \quad (5.5)$$

Where $\mathbf{P}_{0,i}$ is the a priori covariance matrix of the i -th moon and $\mathbf{P}_{0,J}$ is the a priori covariance matrix of Jupiter. These a priori covariances are actually "stabilized" covariances obtained from the following a priori values: for the moon, a linear position uncertainty of 15km in each RSW direction and for the velocity we chose a priori values of 0.15,1.15,0.75m/s in each RSW direction respectively. For Jupiter we used an a priori position uncertainty of 1km (or 10 km) in RSW and a velocity uncertainty of 0.1m/s in each RSW direction. More information on the way the stabilized covariances are obtained can be found in the appendices. Since the observation bias are also parameters to be estimated, the shape of the a priori covariance matrix is the following:

$$\mathbf{P}_0 = \begin{bmatrix} \mathbf{P}_{0,i*} & 0 & 0 \\ 0 & \mathbf{P}_{0,J*} & 0 \\ 0 & 0 & \mathbf{P}_{0,bias} \end{bmatrix} \quad (5.6)$$

Where $\mathbf{P}_{0,i*}, \mathbf{P}_{0,J*}$ are 6×6 stabilized a priori covariances (contain correlation terms) and $\mathbf{P}_{0,bias}$ is a 4×4 matrix containing the a priori biases for each data type:

$$\begin{bmatrix} \alpha_{0,occ} & 0 & 0 & 0 \\ 0 & \delta_{0,occ} & 0 & 0 \\ 0 & 0 & \alpha_{0,VLBI} & 0 \\ 0 & 0 & 0 & \delta_{0,VLBI} \end{bmatrix} \quad (5.7)$$

Where the pair $(\alpha_{0,occ}, \delta_{0,occ})$ are the biases for the stellar occultation and $(\alpha_{0,VLBI}, \delta_{0,VLBI})$ for the VLBI data respectively. The a priori constrain on the stellar occultation bias is 4 mas (or $1.93925472 \times 10^{-8}$ radians) in both right ascension and declination, while for the a priori bias for the VLBI data we used 0.5 nrad in both right ascension and declination.

Weight matrix

The weigh matrix W is defined as the inverse of the measurement noise covariance matrix. This is done in order to minimize the trace of the error covariance matrix. In this work, we define the noise

equal to the accuracy of the measurement. Clearly, the shape of the weight matrix is the following:

$$\mathbf{W} = \begin{bmatrix} \sigma_{occ}^{-2} & 0 \\ 0 & \sigma_{VLBI}^{-2} \end{bmatrix} \quad (5.8)$$

Where $\sigma_{occ}, \sigma_{VLBI}$ are 4.84×10^{-9} rad for stellar occultation (both right ascension and declination) and 0.5×10^{-9} rad for VLBI respectively (both right ascension and declination).

5.3.4 Moon Dynamics

The dynamical parameters of the Galilean moons studied in this work come directly from SPICE kernels.

Acceleration model

When propagating the dynamics of the single moons we took into account the following accelerations:

1. the mutual spherical harmonic acceleration between Jupiter and the moon. With the gravity field of Jupiter expanded to degree 2 and order 0, and that of the moon expanded to degree and order 2;
2. for Jupiter, we considered the point mass accelerations due to Saturn and the Sun;

Where the gravity field of the bodies is expressed in terms of expansion of spherical harmonics functions [8]. The general shape is defined as follows:

$$U(\mathbf{r}, \phi, \lambda) = \frac{\mu}{r} \left\{ 1 + \sum_{l=2}^{\infty} \sum_{m=0}^l P_{lm}(\sin \phi) \left(\frac{r_{ref}}{r} \right)^l [C_{lm} \cos m\lambda + S_{lm} \sin m\lambda] \right\} \quad (5.9)$$

Where r_{ref} is the equatorial radius of the body studied, $\mathbf{r}, \phi, \lambda$ are the radial position, latitude and longitude respectively, $P_{lm}(\sin \phi)$ is the associated Legendre polynomial of degree l and order m ; C_{lm} and S_{lm} are the coefficients of the gravity harmonics which have to be determined experimentally. The mutual spherical harmonic gravity acceleration computes the acceleration exerted by a body B on a body A where the influence of the gravity field of body A have been taken into account. This model includes the couplings between the mass of each body and the gravity field coefficients of the other body [2] [54]. This acceleration model in Tudat combines the spherical harmonic accelerations of the two bodies on each other. The direct acceleration with respect to an inertial origin is computed from:

$$\mathbf{a} = -\frac{\mu_B}{r^2} \hat{\mathbf{r}} + \mathbf{R}^{(I/B)} \nabla^{(B)} U_B(\mathbf{r}) - \frac{\mu_B}{\mu_A} \mathbf{R}^{(I/A)} \nabla^{(A)} U_A(-\mathbf{r}) \quad (5.10)$$

Where U_B, U_A are the spherical harmonic fields of bodies B, A ; $\mathbf{R}^{I/B}$ the rotation matrix, $\nabla^{(*)}$ is the gradient operator in a frame fixed with the body.

Rotation model

We used as rotation model the synchronous rotation model. In this case the rotation of a moon is defined from its relative orbit with respect to the central body, in this case Jupiter. Moreover, the body-fixed z axis is always perpendicular to the orbital plane along the direction of $\mathbf{x} \times \mathbf{v}$ and the body-fixed y axis completes the right handed reference frame. The synchronous rotation model is very useful when approximating the rotation of tidally locked natural satellites like the Galilean moons. We show the effect of the synchronous rotation model by plotting as an example the latitude and longitude angle of Jupiter with respect to Io, propagated for two years.

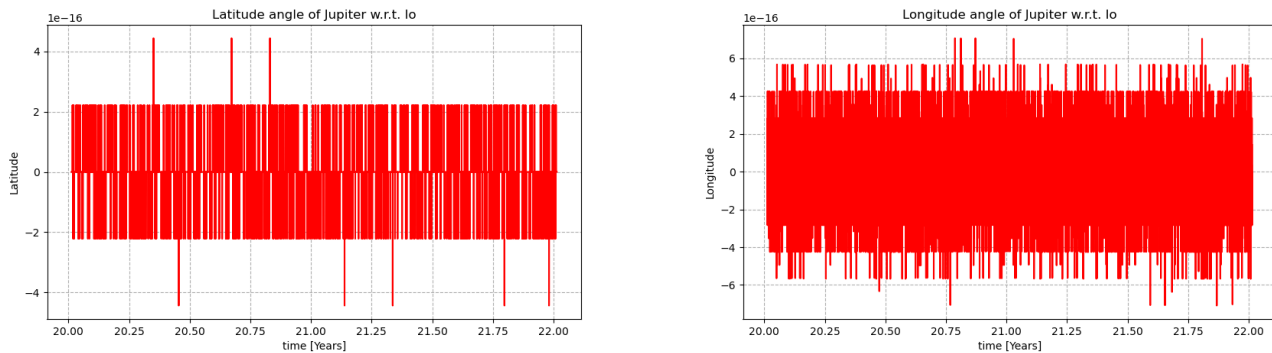


Figure 5.2: LEFT: Latitude RIGHT: Longitude; the scale is in the order of 10^{-16}

As we can see, both latitude and longitude are at about 0. The small oscillations with a magnitude in the order of 10^{-16} are negligible and due to integration errors.

5.3.5 Propagation and Integration

As already mentioned in previous chapters we used a translational propagator to propagate the state vector of the bodies. Here the state vector is defined by the combination of the integrated bodies and their central body, the combination of which define the relative translational states for which a differential equation is to be solved. The specific formulation used in this work is the Cowell propagator, which is the most used one. Let us briefly discuss Cowell's formulation and Cowell's method before discussing the numerical integration method used.

according to Cowell's formulation, is it possible to account for perturbations is to add the perturbing accelerations to the two-body equation in such a way to produce a more accurate equation of motion [38]:

$$\ddot{\mathbf{r}} = -\frac{\mu}{r^3}\mathbf{r} + \mathbf{a}_{perturbed} \quad (5.11)$$

Where $\mathbf{a}_{perturbed}$ is the total acceleration caused by other forces exerted on the body. Following, Cowell's method is a finite difference technique to accomplish the integration. In the most simple

case, Cowell's propagator is defined as follow:

$$\mathbf{x}_{BA} = \begin{pmatrix} \mathbf{r}_{BA} \\ \mathbf{v}_{BA} \end{pmatrix} \quad (5.12)$$

Where \mathbf{x}_{BA} is the state of a body A with respect to a central body B . This will lead to a simple formulation for the state derivative

$$\dot{\mathbf{x}}_{BA} = \begin{pmatrix} \mathbf{v}_{BA} \\ (\ddot{\mathbf{r}}_A)_B \end{pmatrix} \quad (5.13)$$

The equations of motion are then solved using numerical integrators, which are divided in single step and multi step methods. We will quickly point out the main differences between the single-step and multi-step methods.

- The single step methods combine the state at one time with rates at several other times, base on the single state value at time t_0 . The rates are obtained directly from the equations of motion and allow to determine the state of the body at time $t_0 + h$. For single step method, it is usually used a fourth-order Runge-Kutta method. Runge-Kutta methods are widely used as they do not require back values to start the integrator.
- multi step methods in the contrary do an initial estimate (prediction) using previous estimates of the function's rate of change and a second series of of calculations (corrector) use the estimated answer to further refine the result. For this reason, multi step methods are often called predictor-corrector methods. Multi step methods are not self starting as they require some back values to start the algorithm. This methods are usually more accurate and efficient but this also increases the complexity.

In most numerical integration methods some step size techniques are always used. The most common is the fixed step-size which is very useful in case of circular orbits because in this way the step size is kept constant throughout the propagation while variable step-size methods are used in eccentric orbits. We will now explain in details the family of methods (Runge-Kutta) which is the one used in this work.

Runge-Kutta methods

RK (Runge-Kutta) methods, are widely used and they are based on the first-order Taylor expansion:

$$\begin{aligned} y(t_0 + h) &\simeq y_0 + h\dot{y}_0 \\ &= y_0 + hf(t_0, y_0) \\ &= y_0 + h\Phi \end{aligned} \quad (5.14)$$

Where Φ is the increment function. For example, the classical fourth-order Runge-Kutta (RK4) is defined as:

$$\begin{aligned}
 k_1 &= f(x(t_0), y(t_0)) \\
 k_2 &= f(x(t_0 + h/2), y(t_0) + k_1/2) \\
 k_3 &= f(x(t_0 + h/2), y(t_0) + k_2/2) \\
 k_4 &= f(x(t_0 + h), y(t_0) + k_3) \\
 \Phi &= \frac{k_1}{6} + \frac{k_2}{3} + \frac{k_3}{3} + \frac{k_4}{6}
 \end{aligned}
 \tag{5.15}$$

RK4 is able to approximate the exact solution up to order h^4 . In this work we used a Runge-Kutta-Fehlberg 7(8) integrator, which is available in Tudat. RKF78 is a variable step-size method where the step-size can be adjusted based on the required accuracy. We used the RKF78 method as it requires less computational steps than methods of the same order already presented. It works by comparing the solutions of an approximation of the 7th and 8th order to evaluate the accuracy. In this case, both approximations use the same coefficients so it reduces the computational power. Regarding the integration and propagation parameters, we summarize them in the following table:

Integrator used	RKF78
Step size	1800s
Type	fixed
Simulation time	2 years

Table 5.1: Propagation and integration parameters

5.3.6 Observation schedule

We simulated the observations based on the current available data. The stellar occultation prediction of Callisto has been made with the aid of SORA, while the stellar occultation of Io has been already analyzed in the past observational campaign [5]. Regarding the cadence of the VLBI data of Jupiter, we took as reference the current trajectory of JUNO spacecraft, which according to NASA will continue its mission until the end of 2025, thanks to a recent extension. This new extended mission will involve 42 additional orbits, including flybys of Ganymede, Europa and Io [55]. Currently, JUNO is on a very eccentric orbit with an orbital period of 53.4 days and a perijove of about 4,200 km. On June 2021 its orbital period will decrease to 43 days. On September 2022 it will decrease further to 38 days until February 2024 where it will reach 33 days. The following image has been obtained using SPICE toolkit and shows the trajectory of JUNO between 2017 and 2021

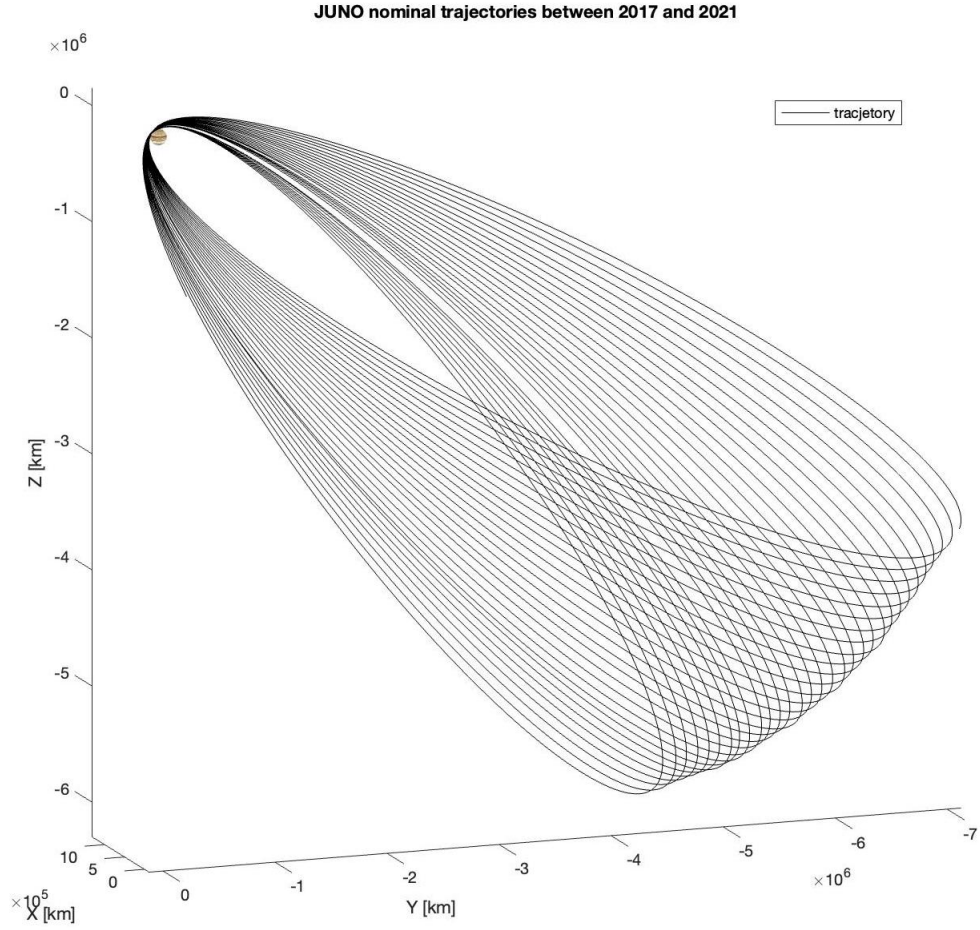


Figure 5.3: trajectory of JUNO spacecraft between 2017 and 2021, obtained with SPICE (DE441 and jup365 spice kernels)

5.4 Covariance propagation

The covariance matrix obtained from the estimation up to time T is calculated as follow:

$$\mathbf{P}(T) = (\mathbf{P}_0^{-1} + \mathbf{H}^T(T)\mathbf{W}(T)\mathbf{H}(T))^{-1} \quad (5.16)$$

Where $\mathbf{W}(T)$ is the weight matrix and $\mathbf{H}(T)$ is the design matrix. The covariance matrix is then propagated to later times by using the state transition matrix:

$$\mathbf{P}(t) = \mathbf{\Phi}(t, t_0)\mathbf{P}(T)\mathbf{\Phi}(t, t_0)^T \quad (5.17)$$

Where the general shape of the state transition matrix is the following:

$$\Phi(t, t_0) = \begin{bmatrix} \frac{\partial \mathbf{x}_i(t)}{\partial \mathbf{x}_i(t_0)} & \frac{\partial \mathbf{x}_J(t)}{\partial \mathbf{x}_i(t_0)} \\ \frac{\partial \mathbf{x}_i(t)}{\partial \mathbf{x}_J(t_0)} & \frac{\partial \mathbf{x}_J(t)}{\partial \mathbf{x}_J(t_0)} \end{bmatrix} \quad (5.18)$$

with \mathbf{x}_i and \mathbf{x}_J being the state of the i -th moon and the state of Jupiter respectively.

The covariance matrix propagation is handled in Tudat with a dedicated function. The function requires as input the covariance at initial time that will be propagated, the state transition interface that handles the propagation through time, which is the interface to the variational equations of the system dynamics and the times at which the propagated covariance shall be retrieved. The procedure has also been performed manually to double check the results obtained with the Tudat function.

The propagated covariance matrix at each time step is then retrieved in inertial coordinates therefore it is then transformed to the RSW frame by applying the transformation already expressed in 4.2.1. Then, the formal errors are extracted by computing the square root of the main diagonal elements.

To retrieve the propagated uncertainties in terms of right ascension and declination (α, δ) with respect to the geocenter, it is necessary to compute the state of the observed body with respect to the Earth center of mass. In Tudat it is possible to compute the relative position as a dependent variable during the propagation. Once the state of the moon with respect to Earth is obtained, it is possible to apply the transformation of the covariance matrix and express it in terms of right ascension and declination:

$$\mathbf{P}_{\alpha, \delta} = \mathbf{J} \mathbf{P}_{x, y, z} \mathbf{J}^T \quad (5.19)$$

Where \mathbf{J} is the transformation matrix from inertial coordinates of right ascension and declination. The formal errors are then obtained by taking the square root of the covariance matrix at each time step.

$$\sqrt{P_{ii}} = \sigma_i \quad (5.20)$$

5.4.1 Workflow visualization

The toolkit used in this work is TudatPy. Here we highlight the workflow in the estimation of the initial states of the bodies in order to better understand the outputs and the required inputs.

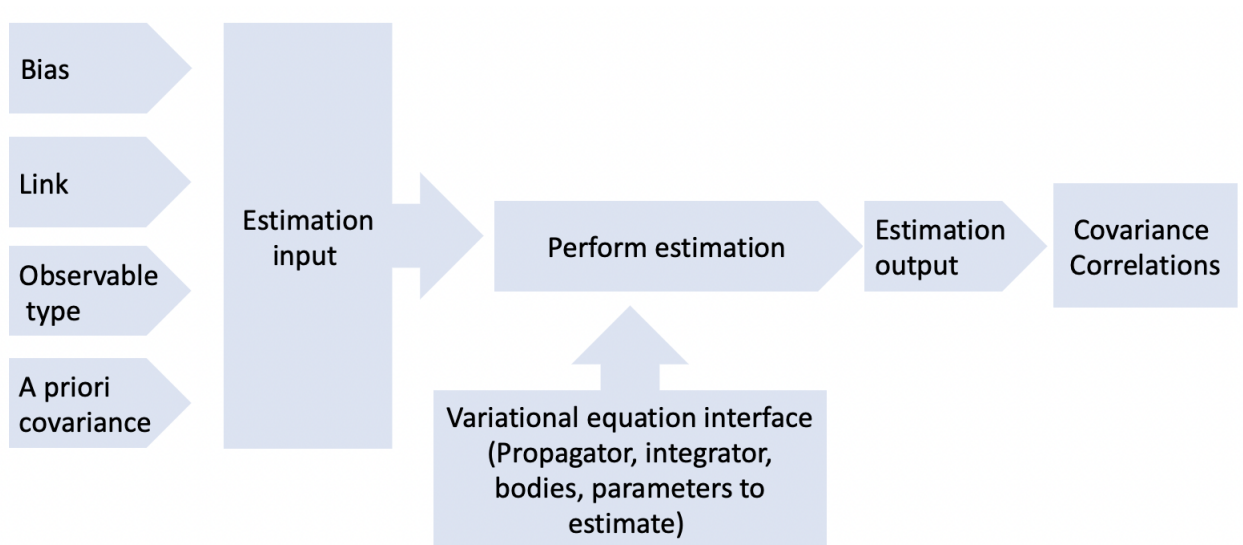


Figure 5.4: Workflow from left to right for the estimation of the initial states; with TudatPy

Where the required inputs are: the bias for the observations, the link between the transmitter and the receiver, the type of observable which in this case is angular position of the observed bodies and the a priori knowledge of the errors in the states. Moreover, it is also required as input for the estimator the variational equation interface which contains the system dynamics. As output of the estimator, along with other parameters, we will retrieve the covariance matrix of the initial states of the bodies.

For completeness, we also provide the workflow for the prediction and analysis of the stellar occultation using the stellar occultation reduction analysis toolkit (SORA).

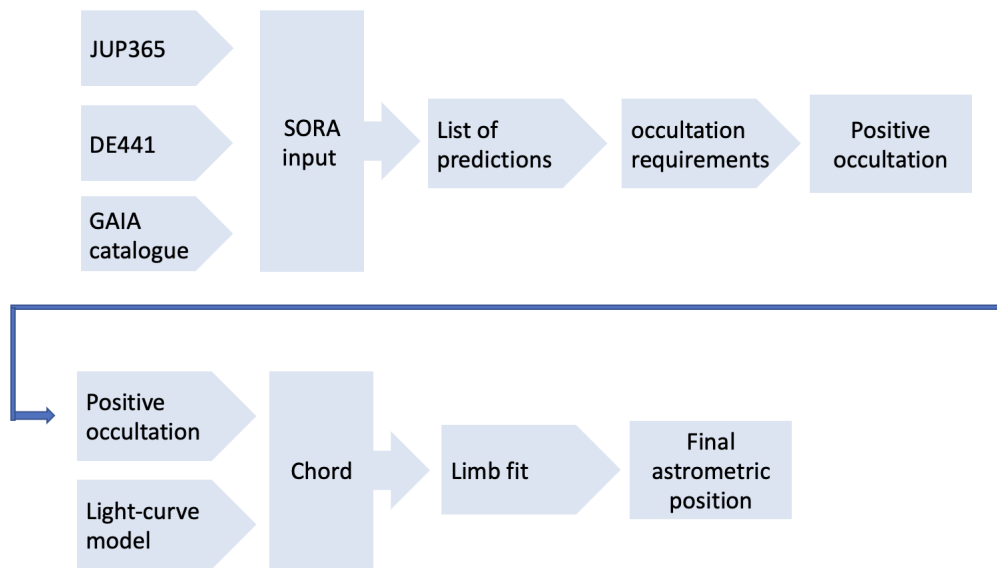


Figure 5.5: Workflow for the stellar occultation prediction and analysis; with SORA

Where for the prediction case, the required input are the ephemeris for the body under analysis (*jup365*), the ephemeris for solar system planets (*de441*) and finally the star catalogue GAIA EDR3 in order to properly find the star for the stellar occultation. The possible stellar occultations are then filtered with our requirements (date, magnitude drop) and we will then finally obtain the stellar occultation we are looking for. As next step, the positive occultation is used as input along with the light-curve model that has been simulated for the specific occultation. The chord is then fitted to the ellipse and we will be able to retrieve the final astrometric position of the celestial body with respect to the geocenter in terms of right ascension and declination (α, δ) .

6

Results

The following section presents the results obtained from the covariance analysis of the estimated states of the moons. The simulated observations are the stellar occultation, predicted using *SORA* and the VLBI observations on Jupiter with a cadence of 53.4 days. The formal errors of the single moons are then propagated along the three RSW directions and by right ascension and declination. We start by highlighting the propagated uncertainties of Callisto and Io. Then we will compare the two cases to discuss similarities and differences. Moreover, we will briefly setup a simulation where the two inner moons are propagated (Io and Europa) to see if an observation on Europa can constrain the state of Io due to the Laplace resonance.

6.1 Callisto analysis

Firstly in this analysis, let us study the prediction of the stellar occultation of Callisto for which the full output of *SORA* can be found in the appendix B, then we will proceed to highlight the different scenarios considered and the obtained uncertainties.

6.1.1 Callisto Occultation

With the aid of the Jovian system ephemeris (*jup365*) it is possible to predict future occultation events by propagating star's position using the Gaia EDR3 catalogue. In combination with *SORA* it was possible to predict a future stellar occultation by Callisto on January 15, 2024. The star and its parameters was identified by Gaia EDR3. The SPKID of Callisto is 504. Observational data are summarized in the following table, where uncertainties in the star position are expressed in milli-arcseconds (mas).

Date and time UTC	Gaia EDR3	α (mas)	δ (mas)	G mag
2024-01-15 06:12:15	73763215746127744	2h15m25.67s (0.019)	12d24m11.15s (0.017)	8.837

Table 6.1: Observation data for body 504

With a propagated magnitude of Callisto at the event of $G = 6.215$ the estimated magnitude drop will be $\Delta mag = 0.083210$.

It is possible to visualize the occultation by generating an occultation map, which requires occultation parameters. Note that no position offsets of Callisto have been considered (6.1).

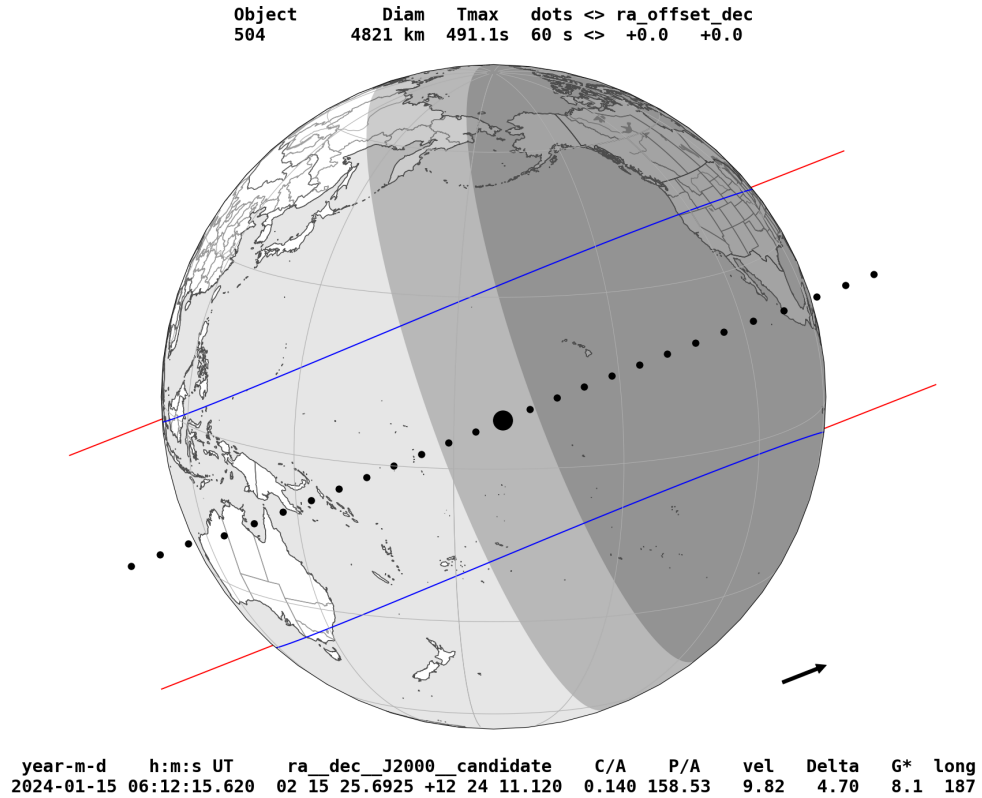


Figure 6.1: Occultation map by 504

In this occultation map the blue lines identify the shadow limits and the black dots are the center of the shadow separated by 1 minute. Also, C/A is the closest approach distance in arcseconds (1 arcsecond = $1/3600^\circ$), P/A is the position angle at closest approach in degrees, *vel* is the velocity of the event in km/s and *mag* is the normalized magnitude to a velocity of 20 km/s.

Based on the occultation map, we simulated an hypothetical observer located in San Diego, California. Here we summarize the fitted times obtained from the simulated light curve.

Station	Immersion time (UTC)	Emersion time (UTC)	Chord length
San Diego, USA	2024-01-15 06:17:43.14	2024-01-15 06:24:38.5	3980.021 km

Table 6.2: Fitted times

We then fitted the limb of Callisto to the stellar occultation chord as seen from San Diego. The red segments represents the 1σ error in each immersion and emersion time.

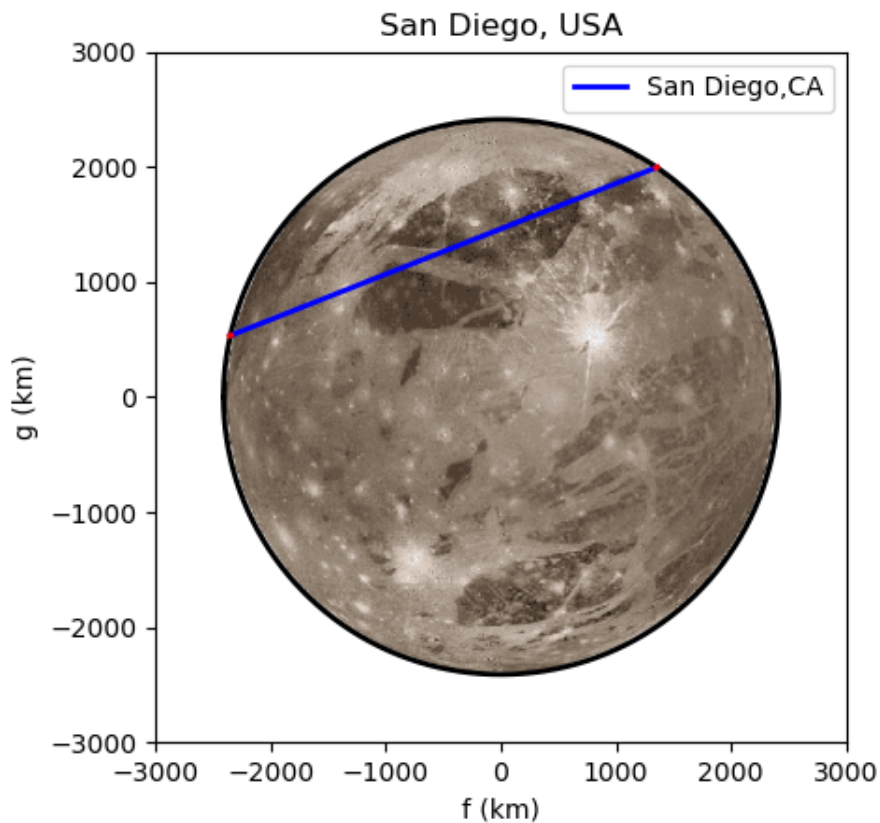


Figure 6.2: Fitted limb on 504

In order to create the stellar occultation light curve model, some physical parameters are required. First, the time axis of the light curve must be projected in the sky plane using the velocity. Then, Fresnel diffraction is applied. The diffraction depends on the object distance (in AU) and the observational wavelength central value λ_0 and its bandwidth $\delta\lambda$. Lastly, the occulted star parameter at the object distance (in km).

For this specific case, the shadow velocity during the occultation is 9.810 km/s and the object

distance is 4.70 AU. The default observational settings have been used: a central wavelength of $\lambda_0 = 0.7$ microns and a bandwidth of $\Delta\lambda = 0.3$ microns. With all the parameters, the mean Fresnel scale can be obtained [56]:

$$F_S = \frac{1}{2} \cdot \left(\sqrt{\frac{(\lambda + 0.5 \cdot \Delta\lambda) \cdot dist}{2}} + \sqrt{\frac{(\lambda - 0.5 \cdot \Delta\lambda) \cdot dist}{2}} \right) \quad (6.1)$$

Which for this simulation is equal to 0.49 km. Finally, the projected stellar diameter at the body distance is 0.40 km. With these parameters, it is now possible to plot the fitted light curve.

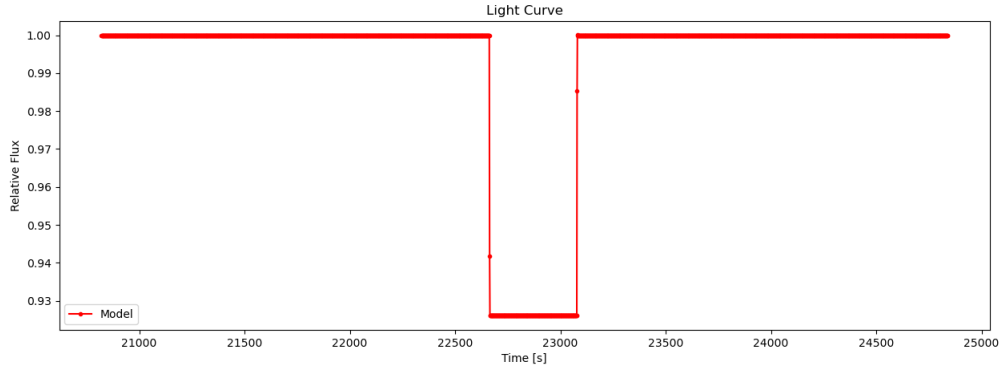


Figure 6.3: Fitted model

Where the x-axis contains the time in seconds after the reference time of 2024-01-15 00:00 UTC and on the y-axis the relative normalized flux. Since the occultation is predicted in 2024, the normalized light curve has been simulated with a Root Mean Square (RMS) noise of $\sigma = 0.02$. We can plot the simulated normalized light curve.

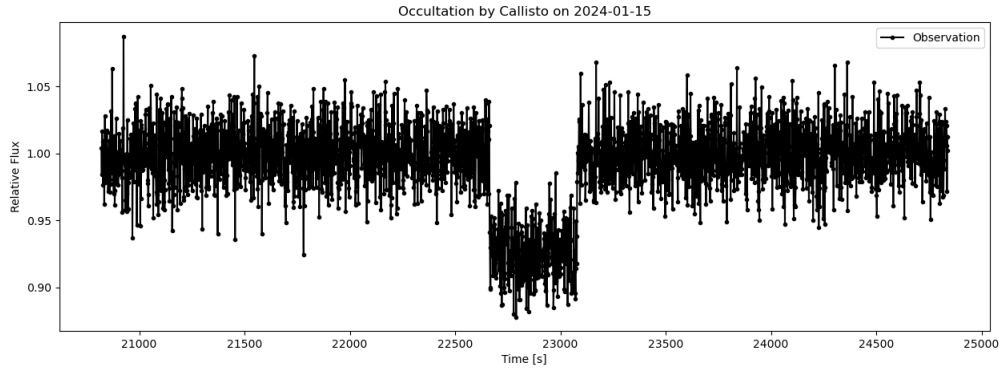


Figure 6.4: Normalized light curve, 504

Further it is possible to plot the fitted model against the normalized light curve.

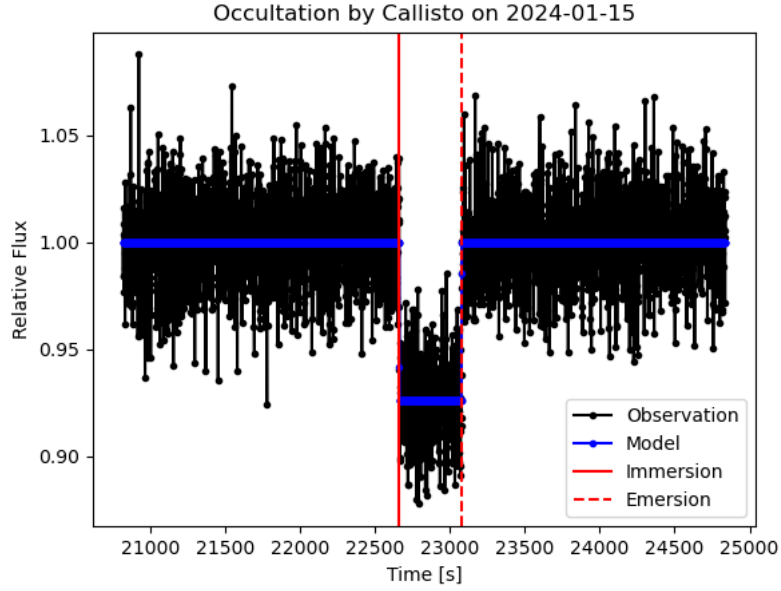


Figure 6.5: Light curve with fitted model

Where the immersion and emersion times are highlighted by vertical solid and dashed lines respectively. The complete post fitted model (geometric, affected by Fresnel diffraction [56] and by the star apparent diameter) can be also be plotted considering only the immersion time.

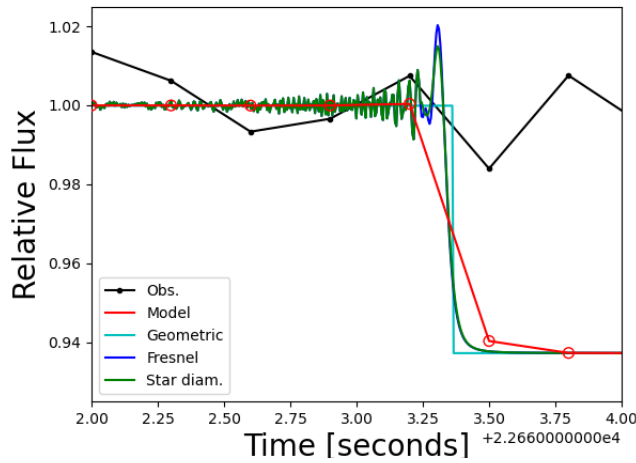


Figure 6.6: Post fitted model

Lastly, we obtained a final astrometric position for the Callisto occultation referenced to the geocenter at the exact time of the occultation event. We stress that this position comes from a simulated lightcurve so the result will be different from the real final position as *SORA* was developed to analyze past occultation and not future ones. Moreover the obtained uncertainties highly depend on the real observation scenario therefore will be highly optimistic.

Body	Date and time UTC	Right ascension	Declination
Callisto	2024-01-15 06:12:15.680	2h15m25s.6959782 (0.203)	12°24'10".98905 (0.175)

Table 6.3: Final predicted astrometric position for Callisto

Now that we have show in details the procedure to obtain lightcurve and the relative chord, let us have a look at the specific geometry at the occultation time. We want to investigate the position of Callisto with respect to Jupiter as seen from Earth. Firstly, let us plot the position of Callisto wrt Jupiter at the time of the stellar occultation

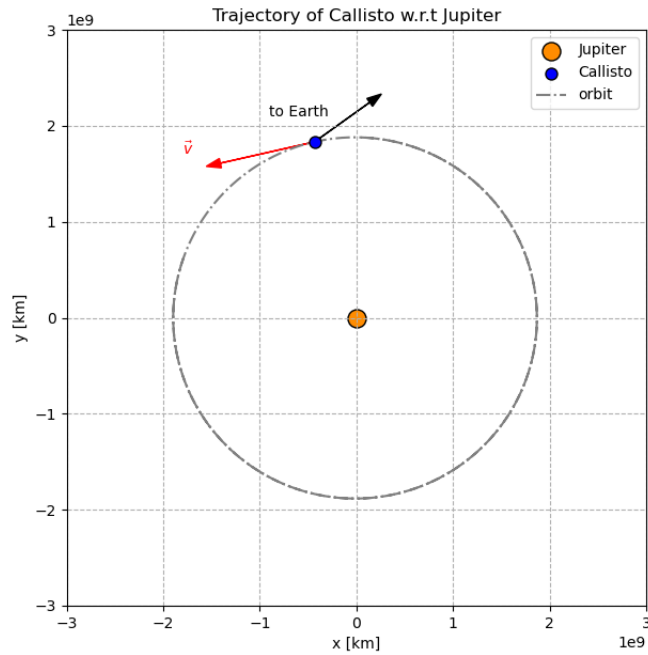


Figure 6.7: Geometry of the occultation of Callisto. The red arrow identifies the direction of the velocity vector of Callisto while the black arrow points towards the Earth

The geometry of the occultation is helpful to understand if the moon is seen from Earth in the direction of its radial direction or velocity vector expressed in the Jupiter barycentric frame.

Assuming that Earth, Jupiter and Callisto are on the same plane, the x, y components of the velocity vector are computed in the following way:

$$\mathbf{v}_{cal}^{(J)} = \frac{x_{cal}}{\sqrt{x_{cal}^2 + y_{cal}^2}}, \frac{y_{cal}^{(J)}}{\sqrt{x_{cal}^2 + y_{cal}^2}} \quad (6.2)$$

Where (x_{cal}, y_{cal}) are the x, y coordinates of Callisto with respect to Jupiter barycentric position. It is possible to calculate the angle between the Earth-Callisto unit vector $\hat{\mathbf{v}}_{cal}^{(E)}$ and the unit vector pointing in the direction of the velocity vector of Callisto with respect to Jupiter $\hat{\mathbf{v}}_{cal}^{(J)}$:

$$\theta_{Cal} = \cos^{-1}\left(\frac{\hat{\mathbf{v}}_{cal}^{(E)}}{\hat{\mathbf{v}}_{cal}^{(J)}}\right) = 157.07^\circ \quad (6.3)$$

From this result and the previous plot we can observe that at the occultation time, the line of sight is almost aligned to the direction of the velocity vector of Callisto. Moreover, Callisto is moving away as seen from Earth. Since the stellar occultation provide the lateral position of the moon, this geometry will constrain mainly the radial component of the position while the along-track component won't be much affected by the observation.

6.1.2 Ephemeris results

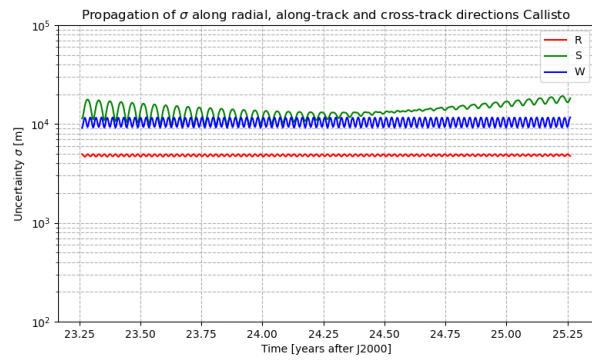
Let us now analyze the resulted formal errors of Callisto obtained from the covariance analysis. We studied three different scenarios: one case where there is no uncertainty in the state of Jupiter (case A), one case where Jupiter has an a priori uncertainty of 1km in RSW directions (case B) and one case where the a priori uncertainty of Jupiter is set to 10km in RSW directions (case C). Moreover, we also took into consideration the case where no data is present for both Callisto and Jupiter. Let us summarize in the following table the different scenarios taken into consideration.

Scenario	Callisto a priori	Jupiter a priori
A	15km, 0.15-1.15-0.75m/s (RSW)	
B	15km, 0.15-1.15-0.75m/s (RSW)	1km, 0.1 m/s (RSW)
C	15km, 0.15-1.15-0.75m/s (RSW)	10km, 0.1 m/s (RSW)

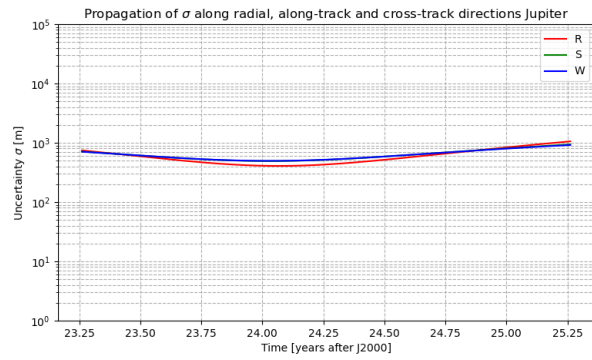
Table 6.4: Callisto analysis of the different scenarios considered in the study

In the next image, the propagated uncertainties have been plotted to highlight the results in the case where no observation data both for Callisto and Jupiter is available.

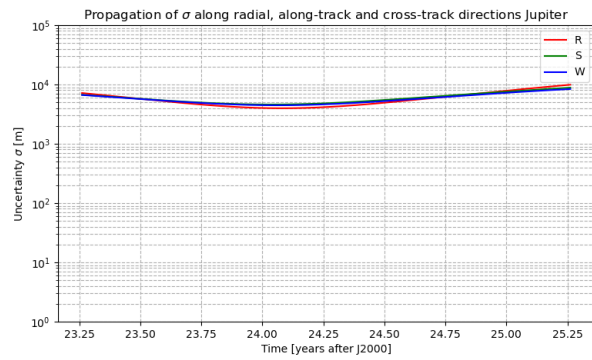
Further, we analyzed the propagated formal errors of Callisto with the different a priori errors of Jupiter while simulating the observations on both bodies, that are stellar occultation and VLBI observables. In the following, the propagated formal errors in RSW position components of Callisto and the absolute correlations of the estimated parameters, which in this case are the initial states and the biases are shown.



(a) case A, perfect knowledge of Jupiter state

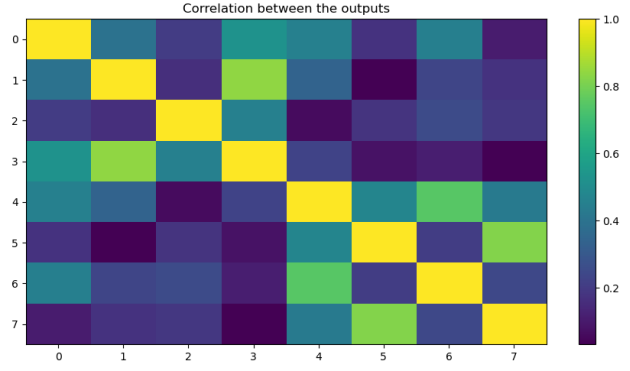
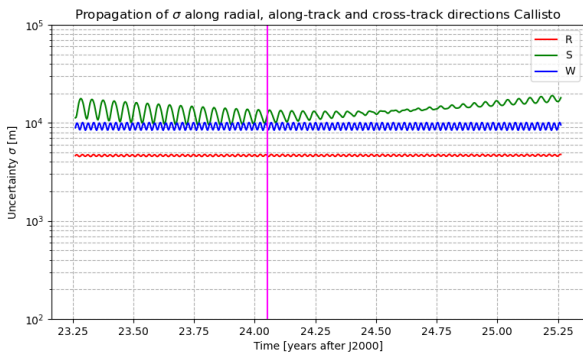


(b) case B, a priori position uncertainty of Jupiter set to 1km in each RSW direction

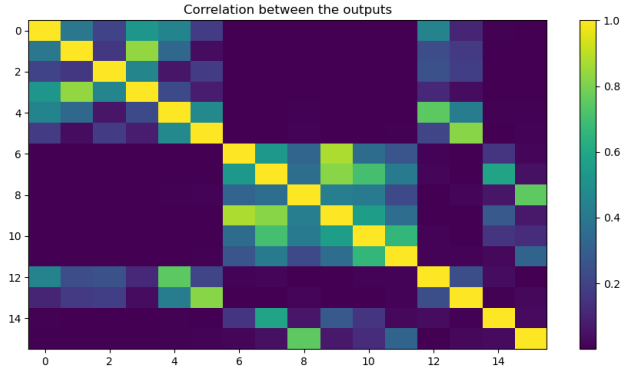
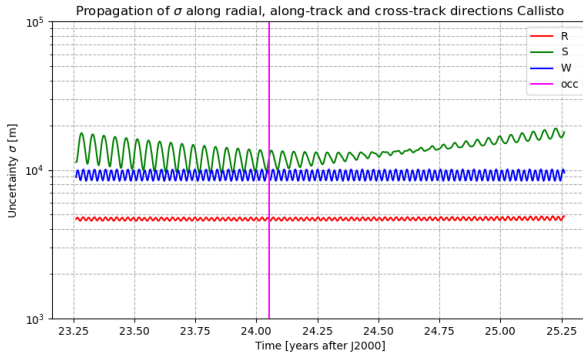


(c) case C, a priori uncertainty of Jupiter set to 10km in each RSW direction

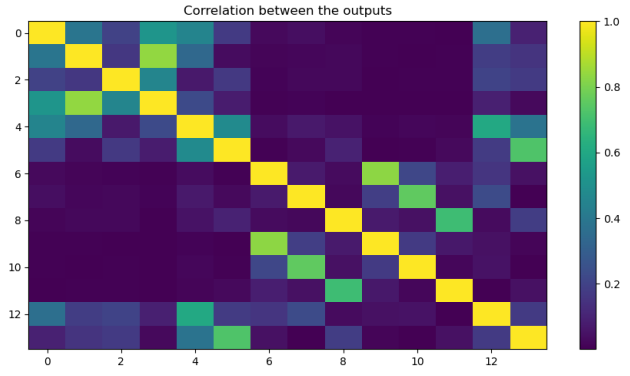
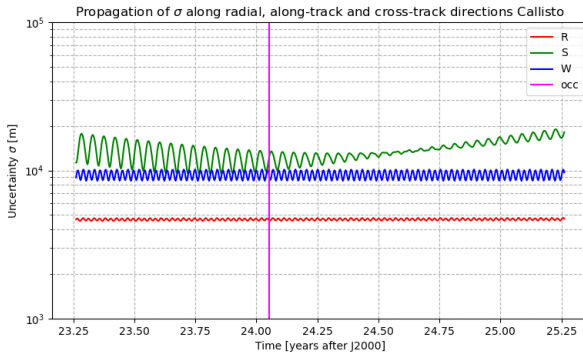
Figure 6.8: Propagated formal errors in case where no data is available



(a) case A, perfect knowledge of Jupiter state. Only stellar occultation



(b) case B, a priori uncertainty of Jupiter set to 1km in each RSW direction. Stellar occultation and VLBI



(c) case C, a priori uncertainty of Jupiter set to 10km in each RSW direction. Only stellar occultation

Figure 6.9: Propagated uncertainties in different scenarios from 6.4. The magenta line indicate the Callisto stellar occultation. For the absolute correlations, elements 0-5 are the state of Callisto, 5-11 Jupiter state, and the other elements on the diagonal are the biases for the stellar occultation and VLBI expressed in terms of right ascension and declination

We can clearly see from 6.9 that due to the particular geometry of the observation, there is no added information to the along-track component of Callisto when performing the stellar occultation. Moreover what we can also observe is that Callisto is not sensitive to Jupiter uncertainties in the case A and B, as only the cross-track components is slightly improved compared to the no data case. We summarize the estimated initial states of Callisto obtained with different settings in the following table:

Scenario	ΔR [m]	ΔS [m]	ΔW [m]
Case A	-314.9	-112.7	-231.9
Case B only occultation	-267.9	-85.8	-199.3
Case B occultation + VLBI	-302.4	-98.2	-225.2
Case C only occultation	-275.0	-84.6	-216.0
Case C occultation + VLBI	-290.5	-98.3	-223.3

Table 6.5: Relative difference in estimated initial states of Callisto expressed in RSW with respect to the case where no data is available. A negative sign indicates an improvement in the uncertainty

When the a priori uncertainty of Jupiter is set to 10km and no VLBI data is available, we can observe that the propagated uncertainties of Callisto are almost unperturbed by the worse error in Jupiter. In fact we get similar values to Case B without the VLBI data. In the situation where also the VLBI and stellar occultation data are present, the propagated uncertainties of Callisto are consistent with the ones of Case B with full data. The average difference with the addition of the VLBI data for case C is quite small with an improvement of about 26m in radial direction, 8.25 m in along-track direction and 18.75m in cross-track direction respectively. This proves that the addition of the VLBI does not provide much additional benefit to the uncertainty of Callisto. It is now interesting to propagate the uncertainties in terms of right ascension and declination. Since the stellar occultation gives this pair of coordinates, plotting the uncertainties in RSW components could hide the behavior of the formal errors. If we now calculate the propagated state of Callisto with respect to Earth barycenter and using the transformation expressed in 4.2.1, we can obtain the propagated uncertainties in terms of right ascension and declination of Callisto when having both the stellar occultation and the VLBI data available for case B.

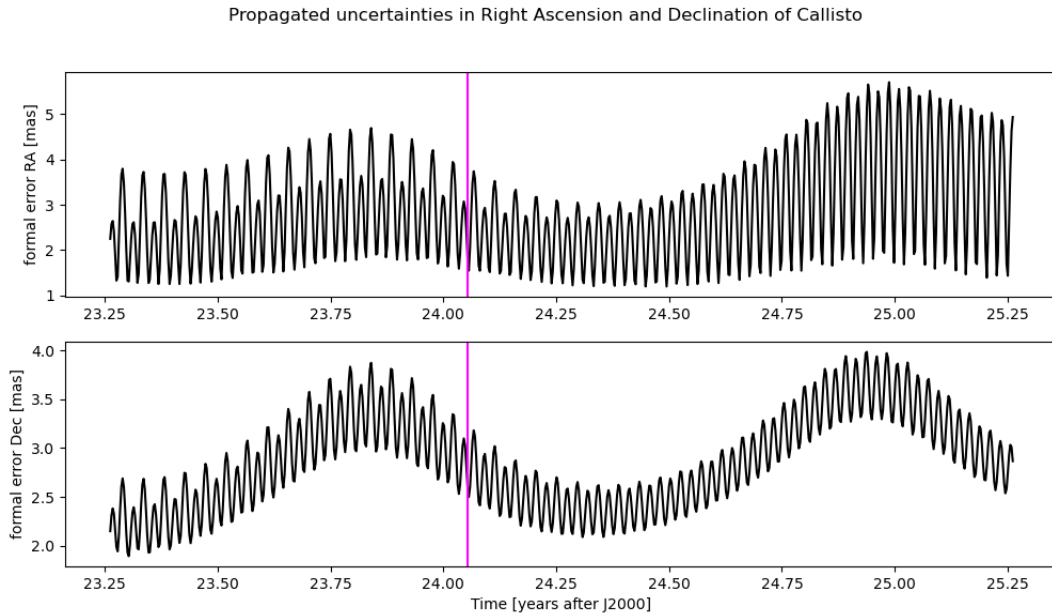


Figure 6.10: uncertainties of Callisto in (α, δ) . The magenta line indicates the stellar occultation

As we can see from the plot, we obtain an uncertainty of 1.5 mas (7.2722052×10^{-9} radians) in right ascension and 2.5 mas (1.2120342×10^{-8} radians) in declination.

6.2 Io Analysis

We now proceed to show the results obtained from the covariance analysis of Io. Here we won't simulate the stellar occultation as it has already been studied by Morgado et al. [5] in the past observational campaign. We recall the final astrometric position obtained from the past stellar occultation of Io, the uncertainty is expressed in brackets by units of mas:

Body	Date and time UTC	Right ascension	Declination
Io	2021-04-02 10:24	21h43m04s.37583 (1.1)	-14°23'58".1536 (0.7)

Table 6.6: Final astrometric position of Io [5]

The stellar occultation happened on 02.04.2021, like we did for the Callisto analysis, let us first display the geometry of the occultation:

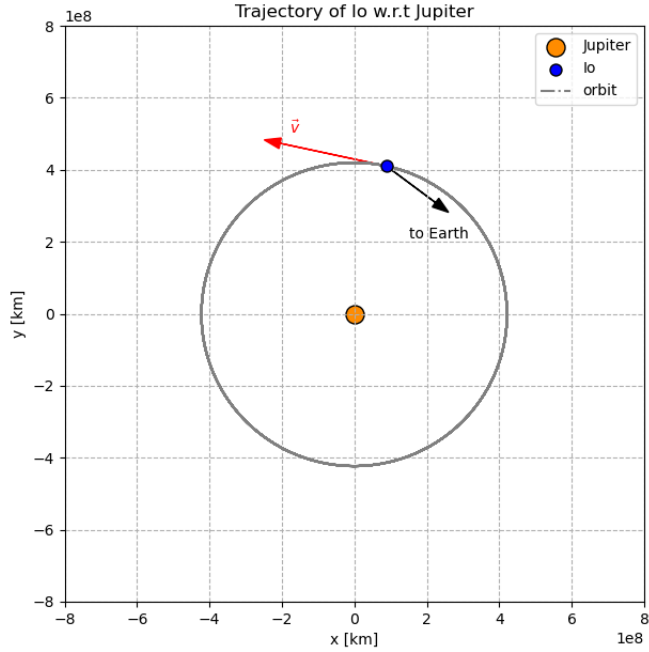


Figure 6.11: Geometry of the stellar occultation of Io

Following the same procedure applied to the Callisto case, we can calculate the angle between the velocity vector of Io with respect to Jupiter and the unit vector pointing towards the Earth center of mass, the angle is found to be:

$$\theta_{Io} = \cos^{-1}\left(\frac{\hat{\mathbf{v}}_{io}^{(E)}}{\hat{\mathbf{v}}_{io}^{(J)}}\right) = 155.33^\circ \quad (6.4)$$

As we can see, the line of sight of the Earth-Io vector is almost aligned with the velocity vector of Io, this will already provide some useful information as the stellar occultation won't be able to constrain much the along-track component of the position.

6.2.1 Ephemeris results

We studied three different scenarios, which are the same for the Callisto analysis. We summarize them in the following table:

We obtained the a priori covariances following the methodology already explained in previous chapters. In the following, we show the propagated uncertainties of Io's position with respect to Jupiter in the case where no data is available.

Scenario	Io a priori	Jupiter a priori
A	15km, 0.15-1.15-0.75m/s (RSW)	
B	15km, 0.15-1.15-0.75m/s (RSW)	1km, 0.1 m/s (RSW)
C	15km, 0.15-1.15-0.75m/s (RSW)	10km, 0.1 m/s (RSW)

Table 6.7: Io analysis of the different scenarios considered in the study

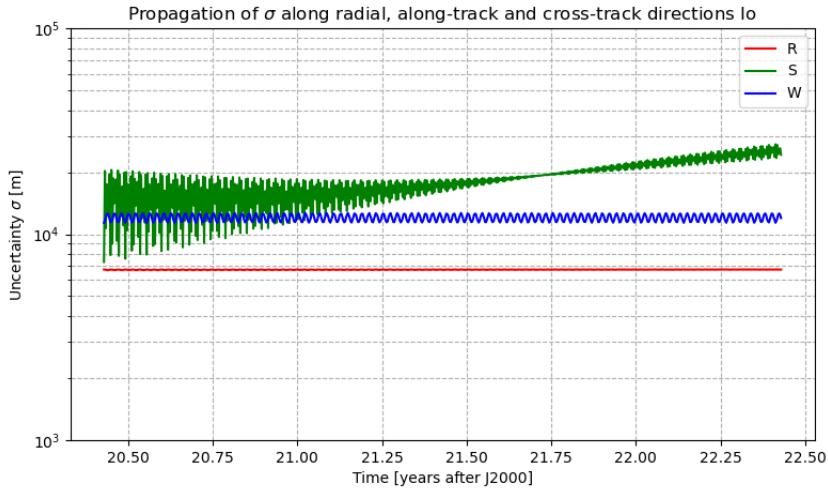
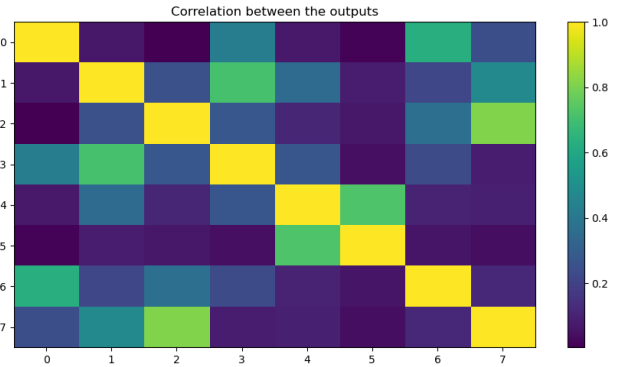
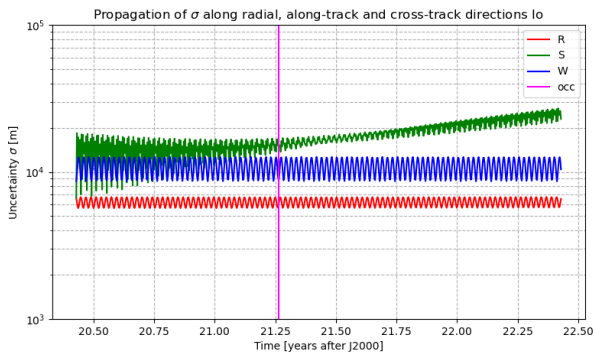
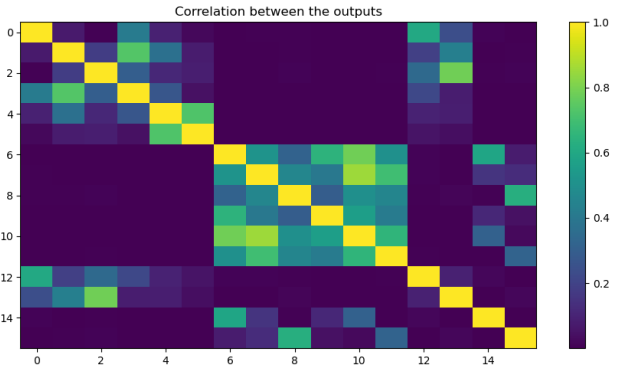
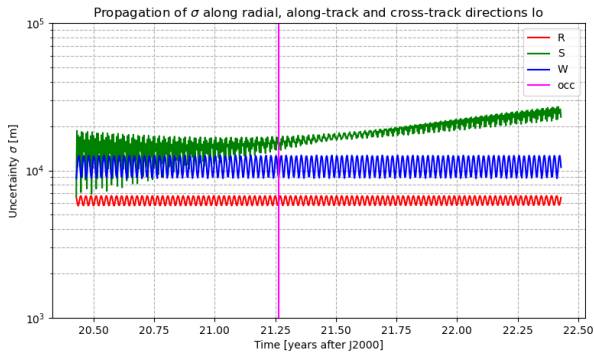


Figure 6.12: Propagated uncertainties of Io's position in the RSW frame

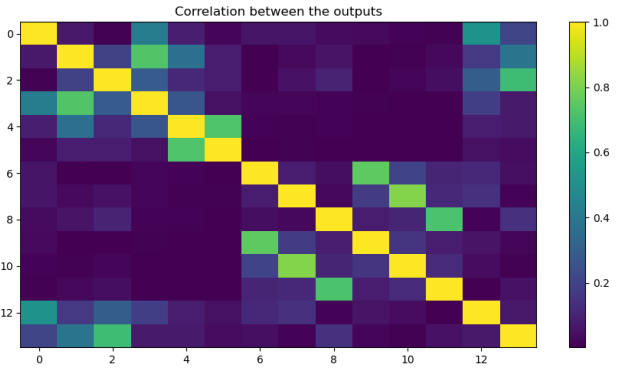
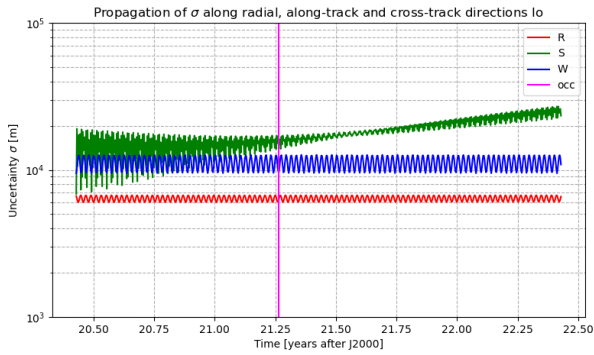
As we can see, with the "stabilized" a priori covariance matrix the along-track and cross-track components are constrained at the 15km level while the radial component is clearly lower, at a 7km level. Instability in the along-track component may be caused by perturbation effects which have not been included in the dynamical model as capturing the full dynamics of the Jovian system is out of the scope of this work. We now highlight the results obtained with the three cases:



(a) case A, perfect knowledge of Jupiter state. Only stellar occultation



(b) case B, a priori uncertainty of Jupiter set to 1km in each RSW direction. Stellar occultation and VLBI



(c) case C, a priori uncertainty of Jupiter set to 10km in each RSW direction. Only stellar occultation

Figure 6.13: Propagated uncertainties in different scenarios from 6.4. The magenta line indicate the Io stellar occultation. For the absolute correlations, elements 0-5 are the state of Io, 5-11 Jupiter state, and the other elements on the diagonal are the biases for the stellar occultation and VLBI expressed in terms of right ascension and declination

We can observe that in the case of both stellar occultation and VLBI data is available, the position uncertainties of Io is comparable to the results obtained when the a priori knowledge of Jupiter is perfectly known. Moreover, as for the Callisto analysis, we can see that even with the worsening of the a priori error in Jupiter the propagated uncertainties of Io are slightly degraded especially in the cross-track component which is much worse compared to the other values. We compared more accurately the formal errors of the estimated initial states of Io's position in RSW. We summarized the differences in each component with respect to the case where no data is available:

Scenario	ΔR [m]	ΔS [m]	ΔW [m]
Case A	-131.1	-684.0	-2708.9
Case B only occultation	-96.7	-655.5	-2677.3
Case B occultation + VLBI	-128.5	-682.5	-2704.9
Case C only occultation	-49.6	-458.2	-1857.6
Case C occultation + VLBI	-127.7	-682.1	-2704.3

Table 6.8: Relative difference in estimated initial states of Io expressed in RSW with respect to the case where no data is available. A negative sign indicates an improvement in the uncertainty

From the table we can clearly observe that in general, the addition of the VLBI data helps to improve the uncertainty of the cross-track component of Io, while all the other components are improved by less extent. We can plot the absolute difference between case C with only the stellar occultation and case C with all the data:

Absolute difference in RSW components when using only occ. or all the data (Jupiter σ 10km)

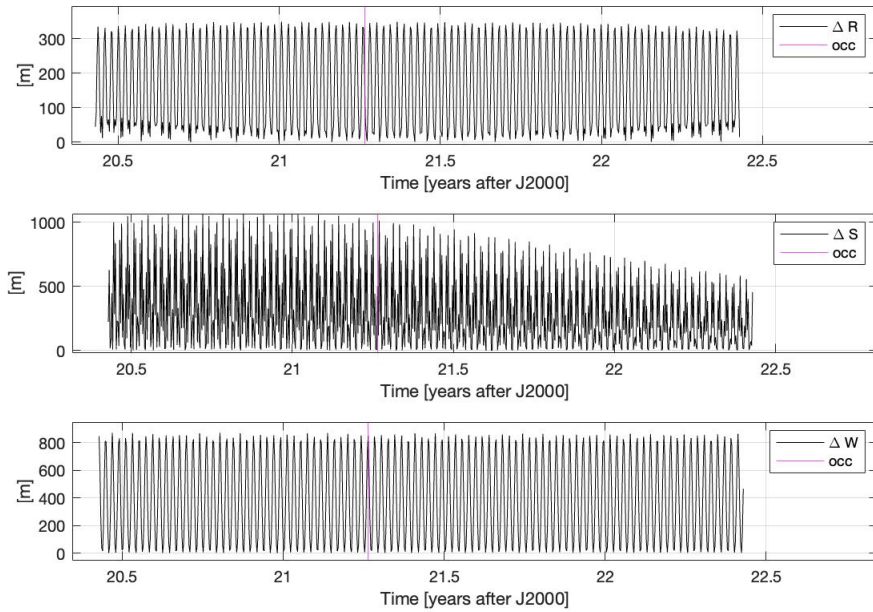


Figure 6.14: Absolute difference between case C (only occultation) and case C (occultation and VLBI)

In the scenario C (Jupiter error 10km) the positive contribution of the VLBI with respect to the case only with the stellar occultation is on average 144m in radial direction, 304.5m in along-track direction and 390.5m in cross-track direction respectively. If we calculate the average difference between case B (Jupiter error 1km) with only the stellar occultation and case B with VLBI and stellar occultation, we see that the contribution of the VLBI data is an improvement of 18m in radial direction, 6m in along-track direction and 16m in cross-track direction respectively.

From case B (1km Jupiter uncertainty, both VLBI and stellar occultation data available) we can derive the propagated uncertainties expressed in terms of right ascension and declination.

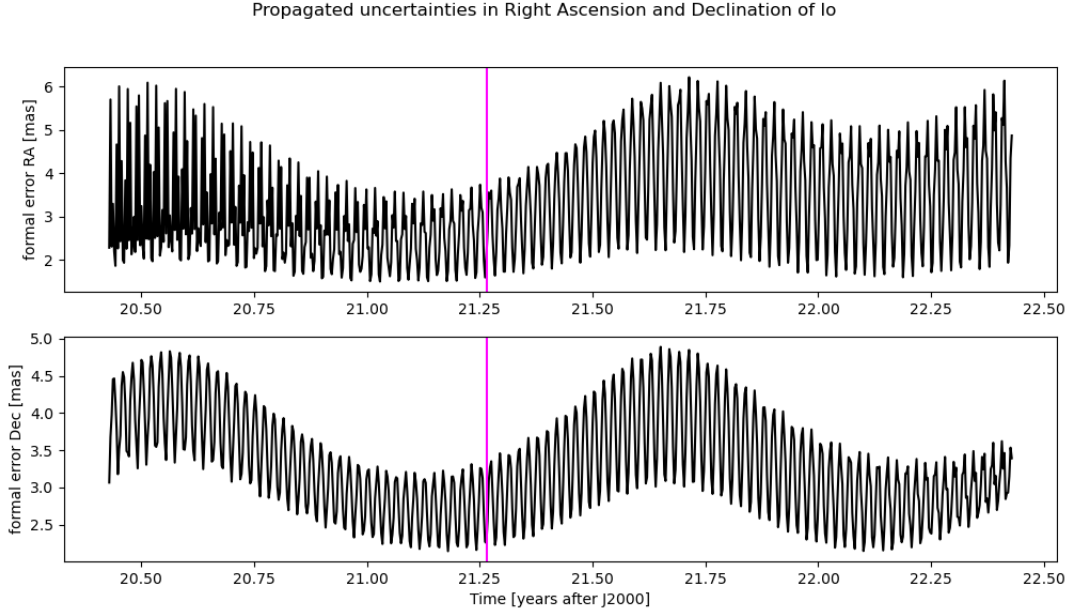


Figure 6.15: Propagated uncertainties of Io expressed in terms of right ascension and declination (α, δ). The magenta line indicates the stellar occultation

It is possible to observe that at the time of the occultation the uncertainty in right ascension is constrained to around 1 mas (4.84×10^{-9} radians) and the declination uncertainty to about 1 mas. The $1 - \sigma$ uncertainties are consistent with the results obtained by the past observational campaign [5]. Also in this situation we can observe from the plot that the formal errors in α, δ are comparable to the ones obtained with Callisto, with these ones being slightly lower.

6.3 Discussion

We will now discuss the results obtained in the above chapter, from the stellar occultation of Callisto to the propagated uncertainties of Callisto and Io, highlighting their similarities and differences. Moreover, we will spend some time to quickly present a possible situation where we demonstrate the coupling in the dynamics between Io and Europa by simulating the two moons together with their respective stellar occultations.

With the aid of SORA, we were able to predict not only the stellar occultation of Callisto but also its shadow on the Earth, this would be extremely helpful in organizing future observational

campaigns for such occultation event and retrieve important data. Moreover, we were also able to simulate the light-curve from a real observational location. Finally we generated a final astrometric position of Callisto with respect to the geocenter (Earth center of mass). The final positions have an uncertainty of 0.203 mas and 0.175 mas in right ascension and declination respectively. In this case, it is important to remember that the obtained uncertainties are very optimistic, as the simulation does not contain real light fluxes and bias were not considered. In the frame of stellar occultations, bias can be in the order of 3-5mas depending on many factors which are impossible to predict and anyways outside the scope of this work. Still, the simulated stellar occultation provides useful insights on the full procedure to obtain a final position and could be used as a reference when organizing and preparing real observations. On a note, since we have also estimated the bias, we found that the estimated bias for the stellar occultation are improved compared to the a priori values, therefore they are not constraint to their a priori values.

The propagated uncertainties of Callisto show that having zero uncertainty in Jupiter or having 1km or 10km a priori uncertainty in Jupiter does not influence much the formal errors. This is verified when simulating only the stellar occultation and with the combination of stellar occultation and VLBI. Such result is verified from the fact that the radial distance between Jupiter and Callisto is very large therefore its influence decreases. In this case the addition of the VLBI observables is not effective in adding information to the uncertainties in Callisto. When having both data type available the formal errors of the initial states are close to the results obtained in Case A (perfect knowledge of Jupiter) with an improvement compared to the no data case of about 302m, 98m and 225m in the radial, along-track and cross-track component respectively. When we simulate only the stellar occultation and we have a large uncertainty in Jupiter see that the propagated formal errors in Callisto are similar to the results obtained in all the previous case with the radial component being the most affected with a degradation of about 40m. In this situation the addition of the VLBI data is important to compensate for this high uncertainty in Jupiter and bring the formal errors in Callisto to about the same level as the scenario of case A and B. In general the main result that we can take from this analysis is that the use of VLBI data does not improve much the results of Callisto. Moreover, we can clearly see that the observation data does not help to constrain the along-track component of Callisto. This is verified from the geometry of the event: the Earth-Callisto vector is almost aligned with the velocity vector of Callisto wrt Jupiter, this confirms the fact that due to this geometry, the stellar occultation measurement is not able to provide additional information to the along-track component. Only with a very accurate occultation measurement (0.1 mas) we are able to constrain the along-track component with a minimum value of the uncertainty of about 3 km at the occultation time while all other components are at a km level.

Moving onto the Io analysis, we can observe a similar pattern compare to the Callisto analysis. In fact, from the results we can see that the influence of Jupiter on the formal errors of Io is quite

small when the a priori constraint of Jupiter is set to 1km. Here, all the components have similar values compared to the ideal case where Jupiter has no uncertainty. On the contrary, we can see that when setting Jupiter with an a priori value of 10km, the effects on Io are much larger than the effects we saw on Callisto. In this situation, the addition of the VLBI data is very important in constraining all components with an improvement of about 80m, 230m and almost 900m in radial, along-track and cross-track direction respectively. This larger contributions should be expected as Io is much closer to Jupiter and therefore it will be more sensitive to its uncertainty compared to Callisto. On this final note, we investigated the effects of a single VLBI measurement performed on Jupiter at the same time of the stellar occultation. Here we consider a measurement with an accuracy of 0.5 nrad and an a priori uncertainty in Jupiter of 10km.

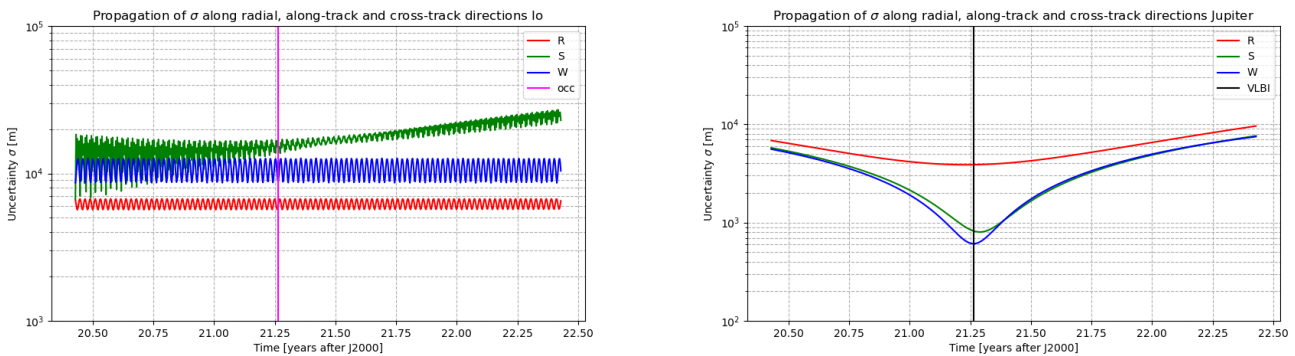
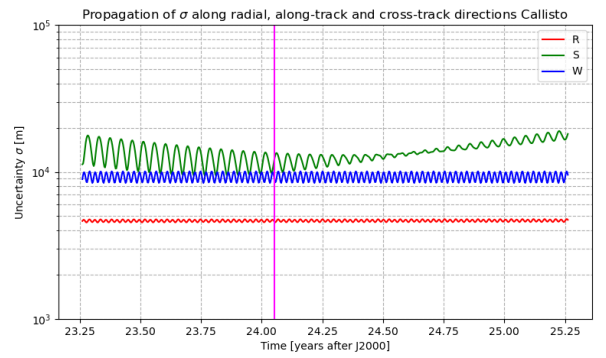
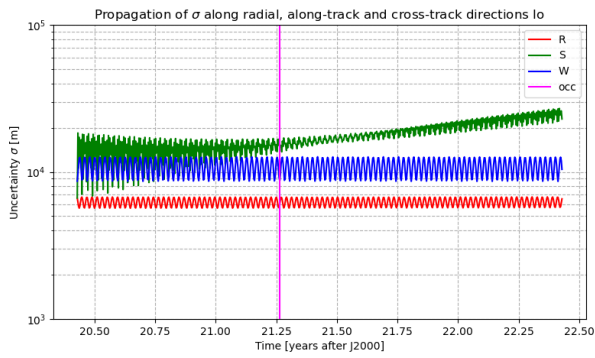
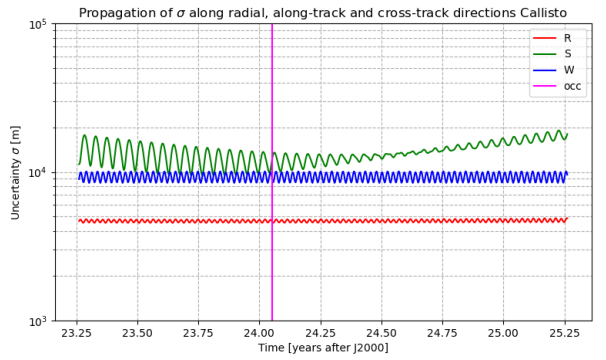
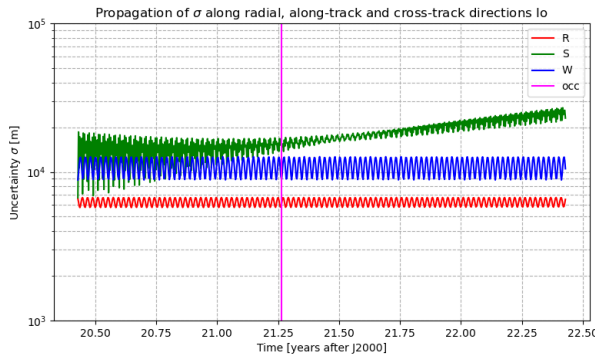


Figure 6.16: LEFT: propagated uncertainties of Io RIGHT: propagated uncertainties of Jupiter; the magenta line indicates the stellar occultation while the black line the VLBI observation

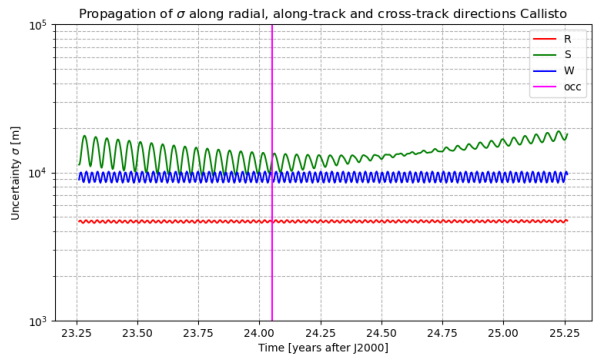
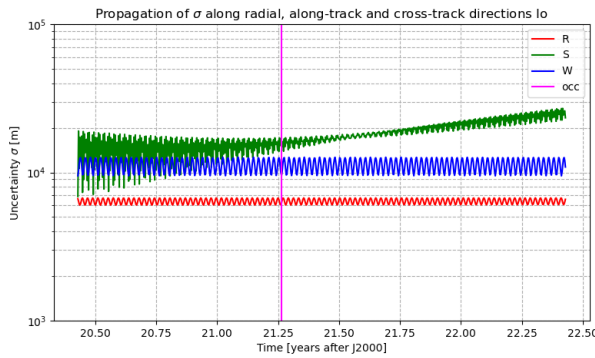
We can clearly see that compared to the case without any VLBI data we have an improvement in formal errors of Io in all three direction. Of course such configuration will be almost impossible to achieve in reality as JUNO orbits are fixed. The idea behind this scenario is to see ideally the improvements that a single VLBI observation can bring to the formal errors of Io. Since we examined the same scenarios on both moons (Callisto, Io) it is helpful to compare them side by side in the different cases. The following page provides a side-by-side comparison of Callisto and Io in Case A, Case B, Case C. Clearly we can see that in Callisto there is no difference between Case A and B (with and without Jupiter). When setting the a priori uncertainty of Jupiter to 10km, Callisto's errors are also almost unperturbed while on Io we see a degradation of the uncertainties which is larger compared to Callisto. Of course this is due to the fact that Io is much closer to Jupiter compared to Callisto.



(a) case A, only stellar occultation



(b) case B, stellar occultation and VLBI (Jupiter error 1km)



(c) case C, only stellar occultation (Jupiter error 10km)

Figure 6.17: Propagated uncertainties in different scenarios of Io (LEFT) and Callisto (RIGHT). The magenta line indicates the stellar occultation

Finally, we can compare the results of Callisto and Io in the situation where both the stellar occultation data and the VLBI data is available (Case B):

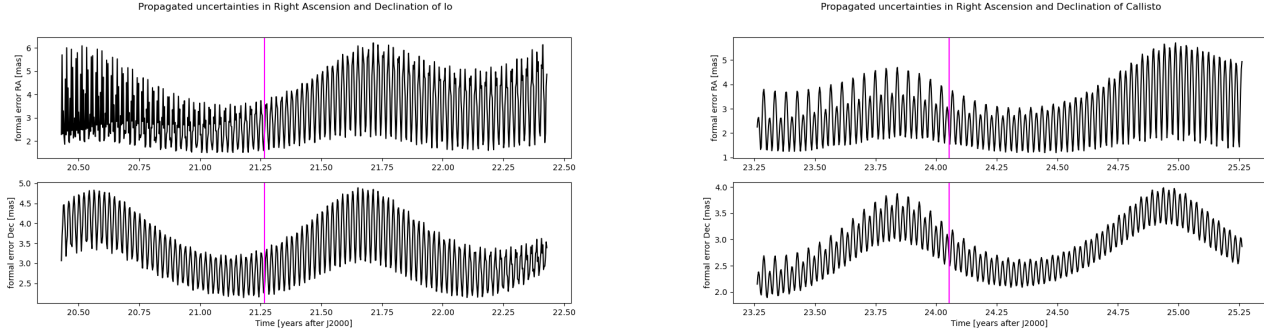


Figure 6.18: LEFT: propagated uncertainties of Io in right ascension and declination RIGHT: propagated uncertainties of Callisto in right ascension and declination; the magenta line indicates the stellar occultation

We can observe that at the occultation time, we obtain similar uncertainties for the right ascension and declination. As for Io we obtain a minimum of 1 mas in right ascension and about 1 mas in declination, while for Callisto we obtain 1.5 mas in right ascension and 2.5 mas in declination. For analysis purposes, we also tried to perform a very accurate stellar occultation observable which we treated as unbiased and with an accuracy of about 0.1 mas (0.4848137×10^{-9} radians). This stellar occultation has been performed alongside the VLBI data of Jupiter. In this case we observed that we were able to also constrain better the along-track component on both moons. In the following image we can see the comparison side-by-side:

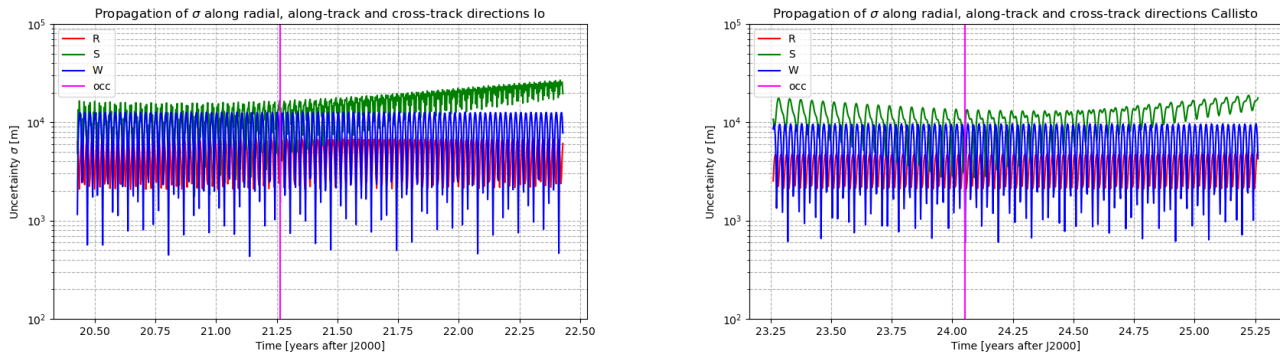


Figure 6.19: LEFT: propagated uncertainties of Io RIGHT: propagated uncertainties of Callisto; the magenta line indicates the stellar occultation

Here we can see that for Io, the uncertainties reach a minimum at the occultation time of about

4km for the along-track component, 2.5km for the radial component and 2km for the cross-track component respectively. For Callisto, we reach a minimum of 3km in the along-track component, 2.5km for the radial component and 2km for the cross-track component. It is important to point out that this kind of scenario is impossible to realize in the real world as such accuracy is not achievable, moreover the stellar occultation measurement will always be subject to biases as many different factors are involved.

6.3.1 Considerations of the coupling between Io and Europa

In this last section we were interested to see if by simulating both Io and Europa together, an observation of Europa could constrain not only Europa's state but also the state of Io. Of course, such analysis is done in a very preliminary way so the results should not be interpreted in a quantitative way but more in a qualitative way since the dynamical model does not include other perturbation effects from Ganymede and Callisto. Still, for our work the assumptions and simplifications in our dynamical model can be considered valid as a preliminary study.

It is important to remember that there exists a strong coupling in the dynamics of the two innermost moons (Io and Europa) due to the Laplace resonance. As we have mentioned in the beginning, the ratio of the mean motions of the two moons should follow the equation:

$$n_{Io} = \sqrt{\frac{\mu_J}{a_{Io}^3}}; \quad n_{Europa} = \sqrt{\frac{\mu_J}{a_{Europa}^3}}; \quad (6.5)$$

Where $\mu_J = 1.26686534 \times 10^{17} m^3 s^{-2}$ is the gravitational parameter of Jupiter and a_{Io}, a_{Europa} are the semi-major axis of Io and Europa respectively. According to our dynamical model, the ratio of the mean motions is found to be:

$$\frac{n_{Io}}{n_{Europa}} = 2.00576 \quad (6.6)$$

As we can see the ratio of the two mean motions is not exactly 2, this is in line with the theory as in order to have resonance, it is sufficient that the ratio of the mean motions is close to 2. This is due to the fact that the equation:

$$n_{Io} - 2n_{Europa} = 0 \quad (6.7)$$

Is not the real resonance, in fact the true resonance also contains the term related to the precession of the pericenter (ϖ) of Io or Europa:

$$n_{Io} - 2n_{Europa} + \dot{\varpi} = 0 \quad (6.8)$$

Which also in this case it will never exactly zero but it will be 0 on average. Now that we explained our assumptions, let us look at one specific scenario of interest. In this case, we investigated if the stellar occultation of Europa performed on 04.06.2019 can constrain the uncertainties of Io. In this scenario we will still have the stellar occultation of Io and the VLBI data from Jupiter. First, let us

plot the propagated uncertainties of Io and Europa in the situation where no data is available.

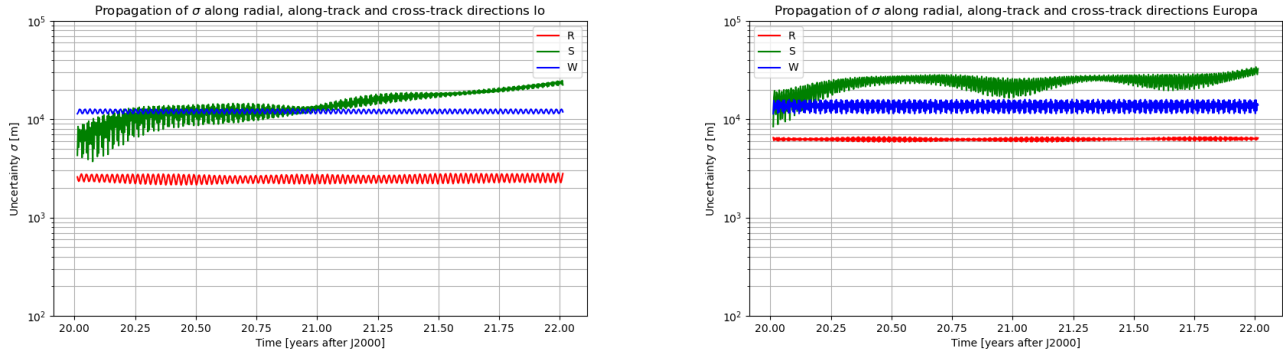


Figure 6.20: LEFT: propagated uncertainties of Io RIGHT: propagated uncertainties of Europa

Now, we proceed to add the stellar occultation data of Europa and Io and the VLBI data of Jupiter using the same values for their accuracy and bias. The procedure is the same already explained in details in the dynamical model. Here the final propagated uncertainties:

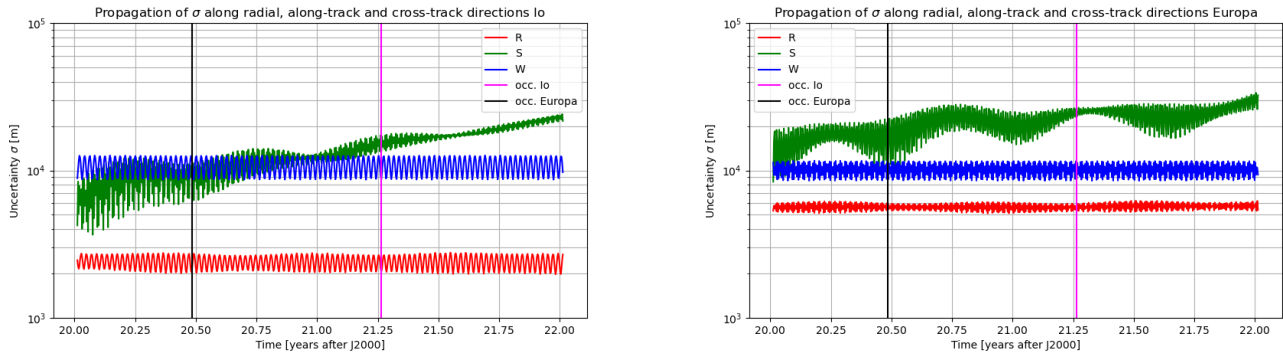


Figure 6.21: LEFT: propagated uncertainties of Io RIGHT: propagated uncertainties of Europa; the magenta line indicates the stellar occultation of Io while the black line the stellar occultation of Europa

Clearly we can see the effects of the stellar occultation of Europa (where the accuracy on Europa’s position improves) on the propagated uncertainties of Io, especially on the along-track component which decreases to about 6km at the occultation time while the radial component is at a 2.5km level and the cross-track at a 10km level respectively. This last results can confirm the bond between the two inner moons due to the Laplace resonance.

7

Conclusions

The objective of this work was to analyze how the addition of VLBI data could help stellar occultation measurements of the natural satellites of Jupiter, in particular on the moons of Io and Callisto. Firstly, we considered the stellar occultation of Io analyzed by Morgado in 2021 [5] as it was part of a past observational campaign. The second stellar occultation used in this work has been predicted and modeled using the stellar occultation reduction analysis toolkit *SORA*. The VLBI data considered comes from JUNO current trajectories as it is the only spacecraft orbiting Jupiter at the time of both stellar occultations. We considered only one accurate measurement per JUNO perijove in order to validate the simplification that we made by not modeling also the spacecraft. From the results we can clearly see how the particular geometry of the occultation scenario can influence the results. In fact, if the Earth-moon vector is aligned or closely aligned to the velocity vector of the moon with respect to its central body we will lose information on the along-track component as stellar occultation provides information on right ascension and declination. Whereas if the Earth-moon vector is aligned with the radial component of the moon with respect to the central body, we would lose information on the radial component but, it was not the case for both moons. However, by inspection, we see that only a very accurate measurement of 0.1 mas can constrain the along-track component even with such geometry. However, such accuracy is impossible to achieve as the Earth-based astrometry are always biased and their accuracy depend much on many factors that have to be analyzed case by case. Moreover, we observed that the VLBI data is not very useful in the situation where Jupiter is known with a 1 km accuracy on both Io and Callisto with Callisto's uncertainties being almost unperturbed. On both satellites we found that the greatest influence of the VLBI data comes when the knowledge of Jupiter is known with a far worse accuracy of about 10 km. This effect is smaller on Callisto due to being further away from Jupiter but on Io this influence is much more important since is the closest satellite from Jupiter. For Io, the addition of the VLBI observables is crucial to constrain all three components of Io's position, in particular the cross-track component which shows an improvement of almost 900m. Moreover, we have also presented the situation where both Io and Europa are propagated together to highlight the coupling between the two moons even when the resonance is not perfect. Here we showed how an accurate measurement of Europa helps

to constrain the along-track component of Io. This results clearly suggest that when simulating for longer period of time, it is very important to take into account any future tracking data that is able to provide accurate information on the dynamics of the two inner moons. It is important to stress that stellar occultations as Earth-based astrometry will be extremely helpful to provide data sets for the position of the Galilean moons in support for future missions like Europa Clipper or JUICE. We finally make some final consideration for a future work on this topic: the dynamics of the moons and mainly Jupiter is influenced by many other parameters that we have not considered like for example the full Jovian system and the external perturbations coming from nearby asteroids which can influence the dynamics of Jupiter. Due to this simplification, the estimated formal errors of the initial state of Jupiter will be very optimistic [3]. Moreover, in our simulations we considered only one moon at a time and only lastly we considered a situation where two moons are simulated together. Of course this simplified dynamics will also produce formal errors of the initial states of the moons to be too optimistic.

Nevertheless, the results obtained in this work provide a useful insight on the contribution of VLBI observables to stellar occultations and how their combination can produce stable data of the Galilean moons. Further investigation should also include more observation data coming from both space probes and future stellar occultations of the Jovian system.

References

- [1] M. Fayolle et al. “Decoupled and coupled moons’ ephemerides estimation strategies Application to the JUICE mission”. In: ().
- [2] Dirx D. et al. “Dynamical Modelling of the Galilean Moons for the JUICE Mission”. In: *Planetary and Space Science* (2016), pp. 82–95.
- [3] Dominic Dirx et al. “On the contribution of PRIDE-JUICE to Jovian system ephemerides”. In: *Planetary and Space Science* 147 (Sept. 2017). DOI: 10.1016/j.pss.2017.09.004.
- [4] Lari G. and Milani A. “Jupiter gravity field estimated from the first two juno orbits”. In: *Planetary and Space Science* (2019).
- [5] B. E. Morgado et al. “Milliarcsecond Astrometry for the Galilean Moons Using Stellar Occultations”. In: *The Astronomical Journal* 163.5 (Apr. 2022), p. 240. DOI: 10.3847/1538-3881/ac6108. URL: <https://doi.org/10.3847/2F1538-3881%2Fac6108>.
- [6] Davies Ashley Gerard. “Volcanism on Io, a comparison with Earth”. In: *Cambridge University Press* (2007).
- [7] Jia X. et al. “Evidence of a plume on Europa from Galileo magnetic and plasma wave signatures”. In: *Nat Astron* 2 (2018), pp. 459–464.
- [8] Andrea Magnanini. “Estimation of the Ephemerides and Gravity Fields of the Galilean Moons Through Orbit Determination of the JUICE Mission”. In: *Aerotecnica Missili & Spazio* (2021), pp. 195–206. DOI: <https://doi.org/10.1007/s42496-021-00090-6>.
- [9] Kivelson M. et al. “Discovery of Ganymede’s magnetic field by the Galileo spacecraft”. In: *Nature* 384 (1996), pp. 537–541.
- [10] Showman Adam P. and Malhotra Renu. “The galilean satellites”. In: *Science* 286 (1999), pp. 77–84.
- [11] Khurana K.K. et al. “Induced magnetic fields as evidence for subsurface oceans in Europa and Callisto”. In: *Nature* 395 (1998), pp. 777–780.
- [12] Malhotra R. “Orbital resonances and chaos in the Solar System. Solar system formation and evolution”. In: *ASP Conference Series* 149 (1998).
- [13] Lainey V. et al. “Strong tidal dissipation in Io and Jupiter from astrometric observations”. In: *Nature* (2009), pp. 957–959.
- [14] Lari Giacomo, Saillenfest Melaine, and Fenucci Marco. “Long-term evolution of the Galilean satellites: the capture of Callisto into resonance”. In: *Astronomy and Astrophysics* (2020).
- [15] B. Morgado et al. “First stellar occultation by the Galilean moon Europa and upcoming events between 2019 and 2021”. In: *Astronomy & Astrophysics* 626 (June 2019), p. L4. DOI: 10.1051/0004-6361/201935500. URL: <https://doi.org/10.1051/2F0004-6361%2F201935500>.

- [16] Sicardy B. et al. “Pluto’s Atmosphere from the 2015 June 29 Ground-based Stellar Occultation at the Time of the New Horizons Flyby”. In: *The Astrophysical Journal Letters* 819.2 (Mar. 2016). DOI: 10.3847/2041-8205/819/2/L38.
- [17] A. Dias-Oliveira et al. “Study of the Plutino Object (208996) 2003 AZ84 from Stellar Occultations: Size, Shape, and Topographic Features”. In: *The Astronomical Journal* 154 (June 2017). DOI: 10.3847/1538-3881/aa74e9.
- [18] R. Leiva et al. “Size and Shape of Chariklo from Multi-epoch Stellar Occultations”. In: *The Astronomical Journal* 154 (Oct. 2017). DOI: 10.3847/1538-3881/aa8956.
- [19] Kiseleva T.P et al. “Results of astrometric observations of Jupiter’s Galilean satellites at the Pulkovo Observatory from 1986 to 2005”. In: *Solar System Research* 42 (Oct. 2008), pp. 414–433. DOI: <https://doi.org/10.1134/S0038094608050055>.
- [20] Tajeddine R. et al. “Cassini ISS astrometry of the Saturnian satellites: Tethys, Dione, Rhea, Iapetus, and Phoebe 2004-2012”. In: *Astronomy & Astrophysics* 575 (Mar. 2015). DOI: 10.1051/0004-6361/201425605.
- [21] L. Lindegren. “Meridian observations of planets with a photoelectric multislit micrometer”. In: *Astronomy & Astrophysics* 57 (May 1977), pp. 55–72.
- [22] Butcher H. and Stevens R. In: *Kitt Peak National Observatory Newsletter* (16 1981), p. 6.
- [23] Assafin M., Camargo J. I. B., and Vieira Martins R. et al. “Gaia Follow-up Network for the Solar System Objects: Gaia FUN-SSO Workshop Proc”. In: (2011).
- [24] Press W. H. et al. “Numerical recipes in C: The art of scientific computing”. In: *Cambridge: University Press* (1992).
- [25] White O.L. et al. “A new stereo topographic map of Io: Implications for geology from global to local scales”. In: *Journal of Geophysical Research (Planets)* (2014). DOI: 10.1002/2013JE004591.
- [26] D. A. Duev et al. “Spacecraft VLBI and Doppler Tracking: Algorithms and implementation”. In: *Astronomy & Astrophysics* 541 (2012). DOI: doi.org/10.1051/0004-6361/201218885.
- [27] D. L. Jones et al. “Astrometry of Cassini with the VLBA to improve the Saturn Ephemeris”. In: *The Astronomical Journal* 149(1) (2014). DOI: doi.org/10.1088/0004-6256/149/1/28.
- [28] C. L. Thornton and J. S. Border. *VLBI Tracking Observables. In Radiometric tracking techniques for deep-space navigation*. Deep-Space Communications and Navigation Systems Center of Excellence Jet Propulsion Laboratory California Institute of Technology, 2000, pp. 47–57.
- [29] O. J. Sovers. *A 5-nrad Extragalactic Source Catalog Based on Combined Radio Interferometric Observations*. Ed. by vol. TDA Progress Report 42-106. 1991. URL: http://tmo.jpl.nasa.gov/progress_report/issues.html.
- [30] C. S. Jacobs et al. *The JPL Extragalactic Radio Reference Frame: Astrometric Results of 1978–96 Deep Space Network VLBI*, ed. by vol. January–March 1998 TMO Progress Report 42-133. 1978. URL: http://tmo.jpl.nasa.gov/%20progress_report/issues.html.

- [31] C. Ma et al. “The International Celestial Reference Frame as Realized by Very Long Baseline Interferometry”. In: *The Astronomical Journal* 116, no.1 (July 1998), pp. 516–546.
- [32] A. E. E. Rogers. “Very-Long-Baseline Interferometry with Large Effective Bandwidth for Phase-Delay Measurements”. In: *Radio Science* 5,no. 10 (Oct. 1970), pp. 1239–1247.
- [33] G. Petit and B. Luzum. *Iers conventions*. Defense Technical Information Center, 2010.
- [34] M. Born and E. Wolf. *Principles of optics: Electromagnetic theory of propagation, interference and diffraction of light*. 7th ed. Cambridge University Press, 2002.
- [35] T. D. Moyer. *Formulation for observed and computed values of deep space network data types for navigation*. Wiley-Interscience, 2003.
- [36] National Radio Astronomy Observatory. *Vlba returning to NRAO, getting technical upgrade*. Jan. 2019. URL: <https://public.nrao.edu/news/vlba-returning-to-nrao> (visited on 06/14/2022).
- [37] D. Jones et al. “VLBA Astrometry of Juno”. In: *Bulletin of the AAS (AAS237 Abstracts)* 53(1) (2021).
- [38] Vallado D. A. and McClain W. D. *Fundamentals of astrodynamics and applications*. 4th ed. Microcosm Press, 2013.
- [39] Chobotov V. A. *Orbital Mechanics*. 3rd ed. AIAA Education Series, American Institute of Aeronautics and Astronautics, Inc., 2002.
- [40] Montenbruck O. and Gill E. *Satellite Orbits: Models, Methods, and Applications*. Springer Verlag, 2000.
- [41] M. Fayolle et al. “Decoupled and coupled moons’ ephemerides estimation strategies Application to the JUICE mission”. In: ().
- [42] Dominic Dirx. *Tudat mathematical model definition*. Jan. 2022. Chap. Variational Equations.
- [43] Milani A. and Gronchi G. *Theory of Orbit Determination. Theory of Orbit Determination*. Cambridge University Press, 2010.
- [44] Curtis H. *Orbital Mechanics for Engineering Students*. 4th ed. Butterworth-Heinemann, 2021. Chap. Geocentric Equatorial Frame.
- [45] M. Fayolle et al. “Analytical framework for mutual approximations Derivation and application to Jovian satellites”. In: *Astronomy and Astrophysics* (2021). DOI: <https://doi.org/10.1051/0004-6361/202141261>.
- [46] Lanyi G., Bagri D. S., and Border J. “Angular Position Determination of Spacecraft by Radio Interferometry”. In: *IEEE Proceedings* 95 (2007), pp. 2193–2201.
- [47] Curkendall D. W. and Border J. S. “Delta-DOR: The One- Nanoradian Navigation Measurement System of the Deep Space Network — History, Architecture, and Componentry”. In: *Interplanetary Network Progress Report* 42 (2013).

- [48] Jones D. L. et al. “Astrome- try of Cassini With the VLBA to Improve the Saturn Ephemeris”. In: *Astronomical Journal* (2015).
- [49] Wu X. et al. “Probing Europa’s hidden ocean from tidal effects on orbital dynamics”. In: *Geophysical Research Letters* (2001), pp. 2245–2248.
- [50] Dirkx D. et al. “Phobos Laser Ranging: Numerical Geodesy Experiments for Martian System Science”. In: *Planet. Space Sci.* (2014), pp. 84–102.
- [51] Rosat S. and Rosenblatt P., Trinh A., and Dehant V.. “Mars and Mercury rotation variations from altimetry crossover data: Feasibility study”. In: *Journal of Geophysical Research (Planets)* (2014).
- [52] Mazarico E. et al. “Simulated recovery of europa’s global shape and tidal love numbers from altimetry and radio tracking during a dedicated flyby tour”. In: *Geophysical Research Letters* (2015), pp. 3166–3173.
- [53] Marty J. C. et al. “Martian gravity field model and its time variations from MGS and Odyssey data”. In: *Planet. Space Sci.* (2009), pp. 350–363.
- [54] Lainey V., Arlot J. E., and Vienne A. “Galilean satellites ephemerides”. In: *VizieR Online Data Catalog* (2004).
- [55] NASA. *NASA’s Juno Mission expands into the future*. NASA, 2021. URL: <https://www.jpl.nasa.gov/news/nasas-juno-mission-expands-into-the-future> (visited on 08/02/2022).
- [56] Gomes-Júnior et al. “SORA: Stellar occultation reduction and analysis”. In: *MNRAS* 511(1) (2022), pp. 1167–1181. DOI: <https://doi.org/10.1093/mnras/stac032>.



Procedure to calculate the stabilized a priori covariance

When propagating the covariances of the bodies, we make use of "stabilized" a priori covariance. In this way, we make sure to also take into consideration the correlation terms and by keeping the propagated uncertainties close to their a priori values. In general, the shape of the a priori covariance matrix is:

$$\mathbf{P}_0 = \begin{bmatrix} \mathbf{P}_{0,i} & 0 \\ 0 & \mathbf{P}_{0,J} \end{bmatrix} \quad (\text{A.1})$$

Where $\mathbf{P}_{0,i}$ is the a priori covariance matrix of the i -th moon and $\mathbf{P}_{0,J}$ is the a priori covariance matrix of Jupiter. Moreover, $\mathbf{P}_{0,i}$ and $\mathbf{P}_{0,J}$ are diagonal matrices which contain only the formal errors. In the following, we explain the technique used to obtain the full a priori covariances for a single body.

Firstly, we assume uncorrelated errors expressed in the RSW frame. This is done because state errors in this reference frame are much less subject to correlations with respect to an inertial case. Then, the covariance matrix \mathbf{P}_0 is transformed from the RSW to the inertial reference frame using the following transformation:

$$\mathbf{P}_{0,xyz} = [J]\mathbf{P}_{0,RSW}[J]^T \quad (\text{A.2})$$

Where J is the rotation matrix from the RSW frame to the inertial frame. To generate correlations we will use this covariance matrix as input of a POD simulation. Here, we will generate cartesian position observables to constrain the body to its a priori values. It is important to note that this type of observable is not realized in reality but is only used for analysis purposes. The data it provides is the inertial (with respect to a global frame origin) cartesian position of the observed body, that is (x, y, z) position. The output covariance matrix is of course calculated using the usual formulation:

$$\mathbf{P}(T) = (\mathbf{P}_0^{-1} + \mathbf{H}^T(T)\mathbf{W}(T)\mathbf{H}(T))^{-1} \quad (\text{A.3})$$

The covariance which is the output of the estimation will then be used as a priori covariance with proper correlation coefficients. It is important to keep the same dynamical model and the same time period. The covariance can be then propagated to any later time following the classical approach:

$$\mathbf{P}(t) = \Phi(t, t_0)\mathbf{P}(t_0)\Phi(t, t_0)^T \quad (\text{A.4})$$

When calculating the stabilized a priori covariance matrix, it is important to note that the a priori uncertainties of Jupiter shall not have effects on the propagated uncertainties of the moon and vice versa, we can prove this calculating the covariance matrix $\mathbf{P}(t)$. First, we recall the shape of the state transition matrix:

$$\Phi(t, t_0) = \begin{bmatrix} \frac{\partial \mathbf{x}_i(t)}{\partial \mathbf{x}_i(t_0)} & \frac{\partial \mathbf{x}_J(t)}{\partial \mathbf{x}_i(t_0)} \\ \frac{\partial \mathbf{x}_i(t)}{\partial \mathbf{x}_J(t_0)} & \frac{\partial \mathbf{x}_J(t)}{\partial \mathbf{x}_J(t_0)} \end{bmatrix} \quad (\text{A.5})$$

Here the terms outside the main diagonal are zero:

$$\Phi(t, t_0) = \begin{bmatrix} \frac{\partial \mathbf{x}_i(t)}{\partial \mathbf{x}_i(t_0)} & 0 \\ 0 & \frac{\partial \mathbf{x}_J(t)}{\partial \mathbf{x}_J(t_0)} \end{bmatrix} \quad (\text{A.6})$$

Since is a diagonal matrix, the transpose is equal $\Phi(t, t_0) = \Phi^T(t, t_0)$. We then calculate the term $\mathbf{P}_0\Phi^T$:

$$\Phi(t, t_0) = \begin{bmatrix} \mathbf{P}_{0,i} \frac{\partial \mathbf{x}_i(t)}{\partial \mathbf{x}_i(t_0)} & 0 \\ 0 & \mathbf{P}_{0,J} \frac{\partial \mathbf{x}_J(t)}{\partial \mathbf{x}_J(t_0)} \end{bmatrix} \quad (\text{A.7})$$

From here we can simply calculate the covariance matrix at a generic time step t :

$$\mathbf{P}(t) = \begin{bmatrix} \mathbf{P}_{0,i} \frac{\partial \mathbf{x}_i(t)}{\partial \mathbf{x}_i(t_0)} \frac{\partial \mathbf{x}_i(t)}{\partial \mathbf{x}_i(t_0)} & 0 \\ 0 & \mathbf{P}_{0,J} \frac{\partial \mathbf{x}_J(t)}{\partial \mathbf{x}_J(t_0)} \frac{\partial \mathbf{x}_J(t)}{\partial \mathbf{x}_J(t_0)} \end{bmatrix} \quad (\text{A.8})$$

Clearly we can see that no correlation terms between the moon and Jupiter are present. This will be the final shape of the stabilized a priori covariance matrix.

We can see the effects of having the full covariance versus only the formal errors, here we show the benefit of this technique on Io. We plot the results of the propagated stabilized a priori covariance matrix:

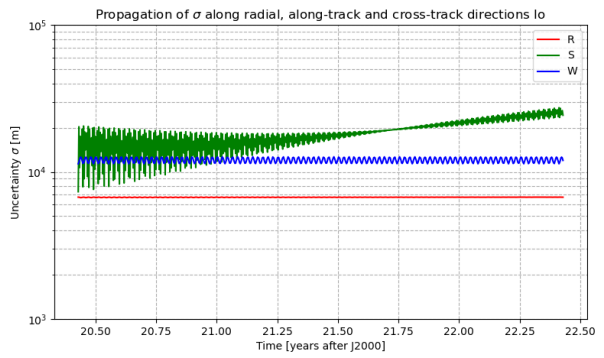
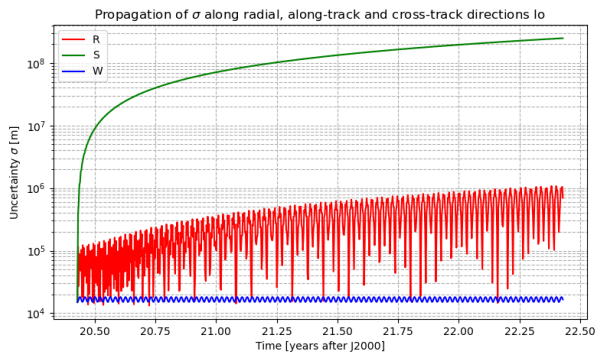


Figure A.1: LEFT: uncertainties propagation without stabilization RIGHT: uncertainties propagation with stabilization

As we can see, the stabilized covariance is much less subject to large fluctuations in the position components. The largest difference can be seen on the along-track and radial component.

B

Output of SORA for the stellar occultation of Callisto

In the following we provide the output of the stellar occultation simulation of Callisto, with all the parameters used. We first define the occultation geometry, star parameters, moon parameters, the result of the simulated observation and the final astrometric position.

Stellar occultation of star Gaia-EDR3 73763215746127744 by Callisto

Geocentric Closest Approach: 0.141 arcsec

Instant of CA: 2024-01-15 06:12:15.680

Position Angle: 158.53 deg

Geocentric shadow velocity: 9.81 km / s

Sun-Geocenter-Target angle: 101.55 deg

Moon-Geocenter-Target angle: 49.74 deg

1 positive observations

STAR PARAMETERS

Gaia-EDR3 star Source ID: 73763215746127744

ICRS star coordinate at J2016.0:

RA=2h15m25.67269s +/- 0.0194 mas, DEC=12d24m11.1506s +/- 0.0167 mas

pmRA=36.496 +/- 0.025 mas/yr, pmDEC=-3.666 +/- 0.021 mas/yr

Gaia-EDR3 Proper motion corrected as suggested by Cantat-Gaudin & Brandt (2021)

Plx=3.9153 +/- 0.0206 mas, Rad. Vel.=20.87 +/- 1.31 km/s

Magnitudes: G: 8.837, B: 9.391, V: 8.962, R: 8.670, J: 7.987, H: 7.780, K: 7.721

Apparent diameter from Kervella et. al (2004):

V: 0.1165 mas, B: 0.1151 mas

Apparent diameter from van Belle (1999):

sg: B: 0.1372 mas, V: 0.1423 mas

ms: B: 0.1277 mas, V: 0.1084 mas

vs: B: 0.2061 mas, V: 0.1850 mas

Geocentric star coordinate at occultation Epoch (2024-01-15 06:12:15.680):

RA=2h15m25.69247s +/- 0.2033 mas, DEC=12d24m11.1198s +/- 0.1748 mas

CALLISTO

Object Orbital Class: Natural Satellite

Physical parameters:

Diameter:

4820.6 +/- 3 km

Reference: Morrison et al. (2000). Icarus 153:157-161,

Mass:

1.0757e+23 +/- 1.9478e+17 kg

Reference: JUP230,

Albedo:

0.17 +/- 0.02

Reference: Morrison et al. (1977). book Planetary Satellites 363-378,

———— Ephemeris ————

EphemHorizons: Ephemeris are downloaded from Horizons website (SPKID=504)

Ephem Error: RA*cosDEC: 0.000 arcsec; DEC: 0.000 arcsec

Offset applied: RA*cosDEC: 0.0000 arcsec; DEC: 0.0000 arcsec

POSITIVE OBSERVATIONS

Site: San Diego, USA

Geodetic coordinates: Lon: -117d09m41s, Lat: 32d43m29s, height: 0.042 km

Target altitude: 33.4 deg

Target azimuth: 263.4 deg

Light curve name: San Diego, USA

Initial time: 2024-01-15 05:47:00.000 UTC

End time: 2024-01-15 06:53:59.700 UTC

Duration: 66.995 minutes

Time offset: 0.000 seconds

Exposure time: 0.3000 seconds

Cycle time: 0.3000 seconds

Num. data points: 13400

Bandpass: 0.700 +/- 0.300 microns

Object Distance: 4.70 AU
Used shadow velocity: 9.810 km/s
Fresnel scale: 0.050 seconds or 0.49 km
Stellar size effect: 0.041 seconds or 0.40 km
Object LightCurve model was not fitted.
Immersion time: 2024-01-15 06:17:43.100 UTC +/- 0.010 seconds
Emersion time: 2024-01-15 06:24:38.500 UTC +/- 0.010 seconds

RESULTS

Ephemeris offset (km): $X = 0.0 \text{ km} \pm 0.0 \text{ km}$; $Y = 0.0 \text{ km} \pm 0.0 \text{ km}$
Ephemeris offset (mas): $da \cos dec = 0.000 \pm 0.000$; $d dec = 0.000 \pm 0.000$
Astrometric object position at time 2024-01-15 06:12:15.680 for reference 'geocenter'
 $RA = 2 \ 15 \ 25.6959782 \pm 0.203 \text{ mas}$; $DEC = 12 \ 24 \ 10.989058 \pm 0.175 \text{ mas}$